*J Neurophysiol* 108: 349–363, 2012.
First published April 11, 2012; doi:10.1152/jn.00153.2012.



# Diode probes for spatiotemporal optical control of multiple neurons in freely moving animals

**Eran Stark, Tibor Koos, and György Buzsáki**
*Center for Molecular and Behavioral Neuroscience, Rutgers University, Newark, New Jersey*

Submitted 21 February 2012; accepted in final form 7 April 2012

**Stark E, Koos T, Buzsáki G.** Diode probes for spatiotemporal optical control of multiple neurons in freely moving animals. *J Neurophysiol* 108: 349–363, 2012. First published April 11, 2012; doi:10.1152/jn.00153.2012.—Neuronal control with high temporal precision is possible with optogenetics, yet currently available methods do not enable to control independently multiple locations in the brains of freely moving animals. Here, we describe a diode-probe system that allows real-time and location-specific control of neuronal activity at multiple sites. Manipulation of neuronal activity in arbitrary spatiotemporal patterns is achieved by means of an optoelectronic array, manufactured by attaching multiple diode-fiber assemblies to high-density silicon probes or wire tetrodes and implanted into the brains of animals that are expressing light-responsive opsins. Each diode can be controlled separately, allowing localized light stimulation of neuronal activators and silencers in any temporal configuration and concurrent recording of the stimulated neurons. Because the only connections to the animals are via a highly flexible wire cable, unimpeded behavior is allowed for circuit monitoring and multisite perturbations in the intact brain. The capacity of the system to generate unique neural activity patterns facilitates multisite manipulation of neural circuits in a closed-loop manner and opens the door to addressing novel questions.

closed-loop control; multichannel recordings; multicolor stimulation; optogenetics

RECENT ADVANCES IN OPTOGENETICS allow expressing light-sensitive channel proteins in specific cell types in virtually any excitable tissue and animal species (Deisseroth 2011). The number of novel opsins and solutions for cell-type specific expression has been rapidly increasing (Fenno et al. 2011; Zhao et al. 2011), and the temporal dynamics of most opsins is within the millisecond range (Boyden et al. 2005; Chow et al. 2010; Gunaydin et al. 2010; Zhang et al. 2007). Several laboratories have developed solutions to deliver optical stimulation to deep brain structures while simultaneously recording neurons (Anikeeva et al. 2011; Gradinaru et al. 2007; Halassa et al. 2011; Royer et al. 2010). However, a number of scientific questions require manipulating neurons in vivo at multiple sites independently at high spatial and temporal resolutions. For example, testing whether and how the rules of spike timing-dependent plasticity (Bi and Poo 1998) apply to the in vivo situation would require manipulation of spike timing of discrete neurons in relation to ongoing brain patterns. Creating "synthetic" receptive fields by pairing native patterns with induced spiking would offer important insights into the mechanisms of neuronal selection (O'Keefe and Nadel 1978). Examining the circuit and behavioral impact of spatiotemporally sequenced activity at different timescales could address the debate on rate vs. temporal coding (Shadlen and Newsome 1998). Finally, a prerequisite for sensory machine-brain interfaces is the ability to generate spatially distributed activation of distinct neuronal groups in real time. Satisfying these requirements is especially challenging for small laboratory rodents, since increasing the weight of the headgear and tether impairs the animal's freedom of movement.

Circuit analysis of neuronal networks requires simultaneous monitoring of the controlled neurons. Current techniques for large-scale recording of multiple single cells in behaving animals include wire tetrodes and silicon probes. Since such electrodes can only record and disambiguate spikes of nearby (up to 60 $\mu$m) neurons (Buzsáki 2004), stimulation of continuously monitored cells requires placing the light source very close to the recording site. However, stimulation through light sources placed on the surface of the brain (Huber et al. 2008) or large fibers placed in the brain parenchyma a few hundred micrometers from the recording sites (Airan et al. 2009; Anikeeva et al. 2011; Cardin et al. 2010; Halassa et al. 2011; Han et al. 2009; Kravitz et al. 2010) inevitably activates many more unmonitored neurons than are being monitored, making the separation between direct and population-mediated effects impossible. Moreover, the high intensity used for the activation of deep neurons may generate superposition of multiple spike waveforms (Royer et al. 2010) and considerable light artifacts (Cardin et al. 2010; Han et al. 2009; Kravitz et al. 2010). Solutions for spatially confined activation of simultaneously monitored neurons were recently described by delivering laser pump-supplied light through optic fibers positioned above the recording sites (Anikeeva et al. 2011; Halassa et al. 2011; Royer et al. 2010). However, applying light at multiple brain sites independently with such approaches would require multiple external laser pumps connected to bulky and stiff fiber bundles, which constrain movement of the animal. Here, we describe how an array of lightweight diodes is coupled to optical fibers. The diode-fiber assemblies are in turn attached to individual shanks of a multishank silicon probe or to wire tetrodes. The diode-probe method permits local (shank- or tetrode-specific) photostimulation and recording of the stimulated neurons without spike waveform superposition or light artifacts. Because the method relies on solid-state light-emitting diode (LED) and laser diode technology, it allows fast multisite, multicolor optogenetic manipulations in behaving animals and concurrent monitoring of the manipulated neurons without limiting free movement of the animal.

Address for reprint requests and other correspondence: E. Stark, Center for Molecular and Behavioral Neuroscience, Rutgers Univ., 197 Univ. Ave., Newark, NJ 07102 (e-mail: eranst@andromeda.rutgers.edu).

  

## METHODS

### *Construction of a Single Diode-Fiber Assembly*

The first step in constructing the multidiode/-electrode array is to couple a diode to an optical fiber (Fig. 1*A*). To enable placing the tip of the fiber close to the recording electrode, multimode fibers with small cores were used [core diameter, 50 $\mu$m; numerical aperture (NA), 0.22; AFS50/125; Thorlabs]. Twenty-five- and one hundred-micrometer fibers were occasionally used, with ~4× lower/higher coupling efficiency and a smaller/larger tip size but similar light intensity. To minimize tissue damage, fiber diameter was narrowed, and the fiber end was morphed into a pointed tip as follows. Fibers were cut to length (2–4 cm), the acrylate jacket at one end was stripped (1 cm; T08S13; Thorlabs), and the stripped end was etched in hydrofluoric acid (Royer et al. 2010) such that only cladding was removed. Hydrofluoric acid was placed in a plastic container (~10 mm deep), covered with a thin layer of mineral oil (~1 mm, reducing acidic fumes and thereby increasing safety and etching accuracy), and several fibers, held by one micromanipulator, were lowered into the acid and retracted at predetermined times (10 min at 8 mm, 5 min at 5.5 mm, and 15 min at 0.5 mm). This generated a stepped profile of the fiber, with the last 5 mm having a diameter of 60–70 $\mu$m and an overetched tip formed into a cone (~12°) at the hydrofluoric acid/mineral oil interface (Fig. 1*A*, *top*). In a variation of this procedure, a nonstripped fiber was pulled (Godwin et al. 1997) with a pipette puller to a 1.2-mm taper (P-2000; Sutter), and the distal end was carefully stripped to enable subsequent attachment to an electrode (see below). In yet another variation, polyimide-clad fibers (with thinner cladding and higher NA; WF61/67/75P37; CeramOptec) were used; here, cladding was removed by immersion in hot sulfuric acid (80° for 10 min in a laminar flow hood) or by the pipette puller. For all fibers, the proximal end was kept jacketed and hand-polished to a symmetrical convex shape (5-$\mu$m polishing paper).

Diodes were prepared for coupling by manually soldering a pair of lightweight flexible wires from which the coating was removed at the very end (~1 mm) to the anode and cathode connections; to prevent

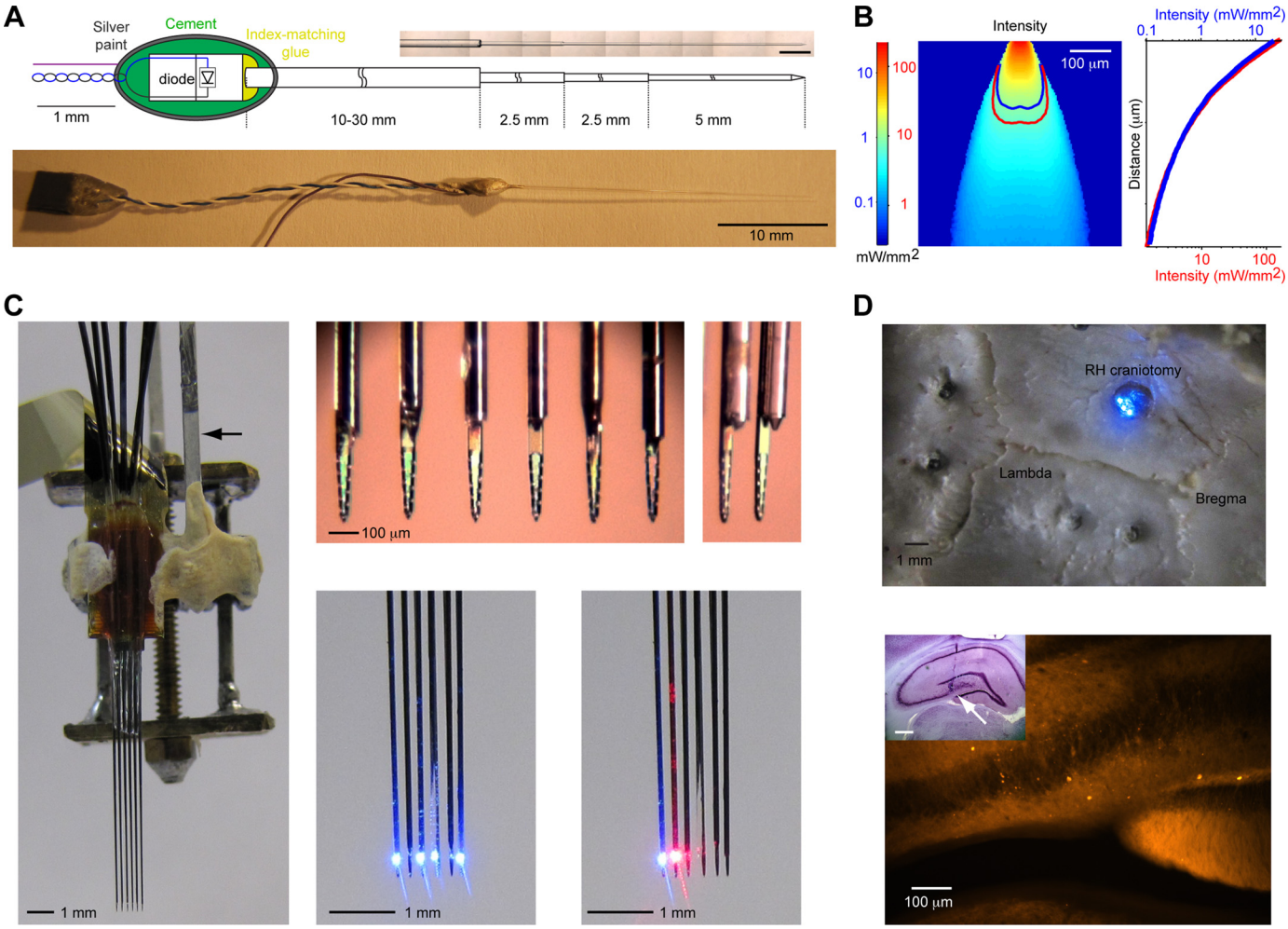


Fig. 1. Multidiode arrays integrated with multielectrode arrays. *A*: structure of a single diode-fiber assembly. The diode is coupled to a 50-$\mu$m multimode optical fiber, etched to a point at the distal end. *Top*: magnified view of the fiber tip; calibration, 1 mm. *B*: light intensity in brain tissue. Light intensity as a function of axial and transverse distance from the fiber tip (*left*) and as a function of axial distance alone (*right*) shown for a blue (red) light source of 40 (300) $\mu$W. Light at intensity > 1 (7) mW/mm$^2$ (for blue/red light; see blue/red lines on *left*) covers a volume of ~0.001 mm$^3$, yielding highly localized photostimulation. *C*: diode-probe example. Six assemblies (4 blue and 2 red) were attached to separate shanks of a 6-shank silicon probe. *Left*: probe on a movable drive; arrow, metal rod used for connecting the diode ends of the fibers. *Top*: magnified frontal view of all 6 shanks (*top middle*) and an oblique view of 2 of the shanks (*top right*). *Bottom middle*: 4 shanks illuminated with blue light. *Bottom right*: 2 adjacent shanks illuminated with blue and red light. *D*: long-term optical stimulation and neuronal recordings. *Top*: explant of a multidiode array after 2 mo of recordings from the right dorsal hippocampus. The diode probe, equipped with 6 light-emitting diode (LED)-fiber assemblies, was left in situ, and 3 nonadjacent shanks were illuminated while photographing the skull from the inside out. *Bottom*: fluorescence image of a coronal section through the hippocampus of the same animal [tdTomato fluorescence, viewed via a rhodamin (RH) filter] and Nissl staining of an adjacent 80-$\mu$m section (*inset*) showing the track of a probe shank ending in CA3c pyramidal layer (arrow; calibration, 500 $\mu$m).

damage to the diodes, care was taken to minimize soldering time to <1 s. In the context of implantable arrays, diodes for efficient coupling to fibers require the following: high light intensity, low current consumption, small emitter size, and light weight. Numerous miniature diodes from various manufacturers were inspected and tested for light-coupling potential with fibers. Commercially available diodes fulfilling the abovementioned requirements include products by Kingbright (465-nm LED; APA1606PBC/Z, APA1606QBC/G; 1.6 × 0.6 mm), OSRAM (470-nm LED; LB P4SG; 2-mm diameter), and Opnext (639-nm laser diode; HL6359MG), among others. The other ends of the wires were soldered to a SIP connector (Mill-Max), twisted, and isolated using hot glue (Fig. 1*A*). Before coupling, the light power of each wired diode was measured: when driven by a calibrated current source (20–60 mA, depending on the diode), these diodes yielded 10–15 mW of light.

For coupling the fiber with the diode, the fiber was held by a micromanipulator enabling 6 degrees of freedom (II in Fig. 2*B*); another micromanipulator (I) held the prewired diode, which was connected to a precision current source. The distal tip of the fiber was positioned close to a light sensor (S130A photodiode; Thorlabs); to prevent direct illumination of the sensor, the fiber was threaded through pinholes in two pieces of black paper (Fig. 2*B*). The diode and fiber were initially oriented such that the fiber was approximately perpendicular to the emitter of the diode, at a distance of <2 mm. This typically generated some visible light output at the fiber tip. Next, the sensor was positioned, and the diode micromanipulator (I) was adjusted in three dimensions to maximize the power while keeping a small gap (10–20 $\mu$m) between the diode and the fiber end. Readings of 15–25 $\mu$W were usually obtained at this stage (coupling efficiency, 0.1–0.15%; blue LEDs; for laser diodes, the efficiency was an order of magnitude higher, ~2.5%). A drop of UV-curable glue (NOA-61; Norland Products) was placed on the fiber-diode interface, the power was measured, and the location was reoptimized. Since the refractive index (RI) of the glue is higher than air (1.56–1.57), the drop of glue reduced Fresnel losses and approximately doubled the acceptance angle of the fiber to skew rays (see below). This resulted in effective doubling of the light output (30–50 $\mu$W for blue LEDs, ~0.25%; laser diodes, ~5%). The glue was then cured by exposure to UV light by a UV gun (ELC-410; Thorlabs; Fig. 2*B*, *right*) for 10 min.

Before attaching the diode-coupled fiber onto a tetrode/silicon probe, the coupling interface was further fortified by a drop of grip cement (Dentsply). The cement also served to isolate the electrical connections of the diode. Isolation quality was checked using an impedance meter at 1 kHz by immersing the entire diode-fiber assembly in saline (0.9%); readings >15 MΩ were accepted. Finally, to prevent electromagnetic transients generated by the diode from affecting the electrophysiological recordings, the assembly was shielded using conductive silver paint (SEMicro), and a ground wire was connected (Fig. 1*A*). A single assembly weighed 100–130 mg.

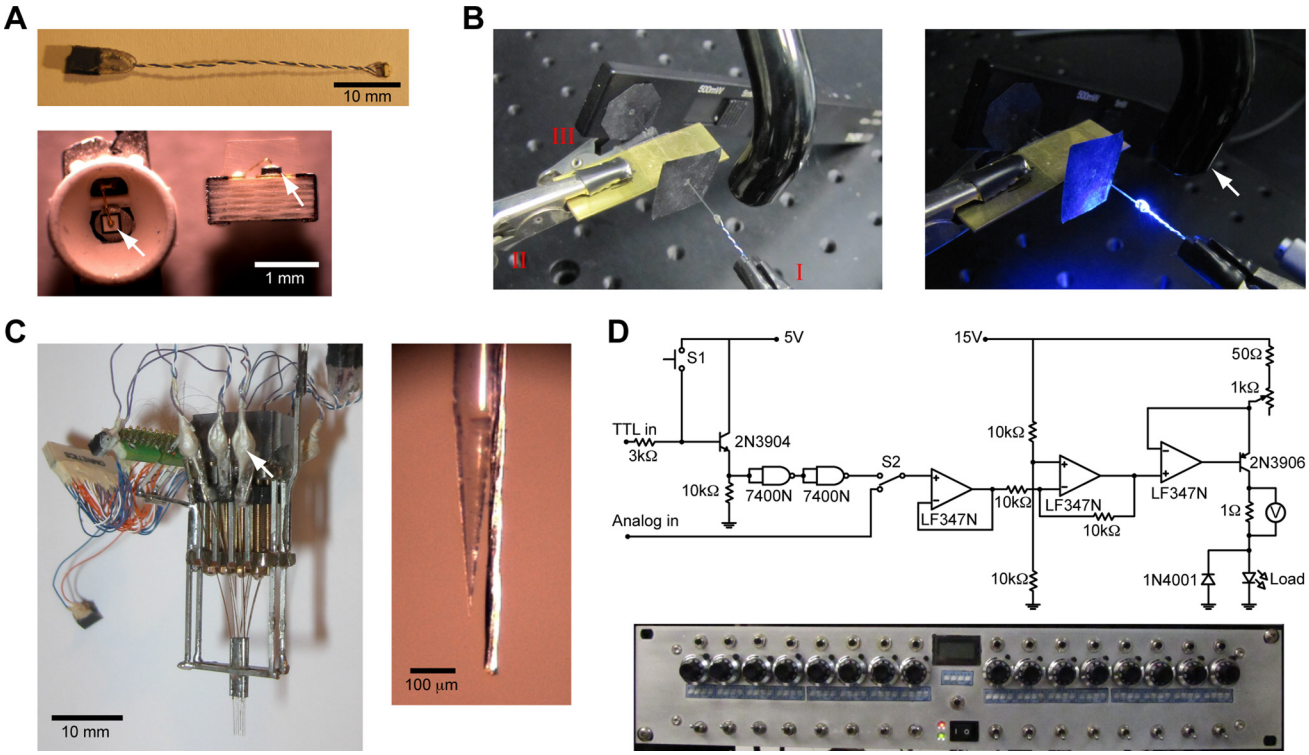


Fig. 2. Diode-fiber assembly construction and driving. *A*: example LEDs. *Top*: wired LED (APA1606QBC/G; Kingbright). *Bottom*: nonwired diodes (LB P4SG, OSRAM; APA1606PBC/Z, Kingbright). Arrows show light emitters. *B*: alignment and coupling of diode and fiber. *Left*: 3 micromanipulators are used: I holds the wired diode; II holds the etched fiber; and III holds a light sensor (S130A; Thorlabs) set to the 100-$\mu$W range. Two pieces of black paper with pinholes are slipped over the fiber and cover the sensor aperture and diode such that the sensor reading is 0 when the diode is not lit. *Right*: following optimization of the relative location of diode and fiber, a drop of UV-curable glue is placed on the interface and cured using a UV light gun (arrow). *C*, *left*: tetrode-based diode probe. Each tetrode is coupled to a diode-coupled fiber (arrow) and mounted on a separate movable drive. *Right*: tetrode attached to a diode-coupled fiber. The tip of a 100-$\mu$m core optical fiber (AFS105/125; Thorlabs) was etched to a cone, and the fiber was coupled to a blue LED. The assembly was then attached, using UV-curable glue, to a tetrode such that the fiber tip was ~100 $\mu$m above the recording end of the wires. *D*: multichannel precision current source. *Top*: schematic of a single channel. The input stage consists of an NPN transistor in an emitter-follower configuration, a digital buffer, a source selector, and an op-amp follower to ensure high input impedance; this enables 3 different operating modes: manual (push button), digital input [transistor-transistor logic (TTL)], and analog input. The current control stage consists of a differential amplifier and a PNP transistor with an op-amp negative-feedback; this yields linear compliance for up to 10-V voltage (*V*) drop at the load while enabling programming relative to ground. *Bottom*: front panel of the rack-mounted device, showing for each channel (from top to bottom) the push buttons, potentiometers, analog input selectors, and analog/digital source selectors.

*Diode Probe: Combining Multiple Diode-Fiber Assemblies with a Multielectrode Array*

Each assembly was attached to a separate shank of a silicon probe (e.g., Buzsaki64SP from NeuroNexus) following previously described procedures (Royer et al. 2010) with a few modifications. First, the probe was cemented onto a movable drive, and a small T-shaped metal rod was cemented to the moving part of the drive for subsequent connection of the diode ends of the fiber (Fig. 1*C*, *left*). Second, each fiber was placed, under microscopic guidance, so the tip of the fiber was ~50 $\mu$m away from the top-most recording site (Fig. 1*C*, *top*); this resulted in a light cone that covered the entire range of recording sites (<200 $\mu$m) immediately below the fiber but did not illuminate nearby shanks or distant loci (Fig. 1*B*). Care was taken to ensure that glue did not flow onto the recording sites or the exposed core at the fiber tip. Fibers were attached sequentially, starting from the lateral shank and continuing toward the middle. After each fiber was attached to the corresponding shank, some more UV glue was deposited on the base of the probe (the part that was not inserted into the brain) and cured. Next, the proximal (jacketed) part of the fiber was bent (<10°), and the diode end of the fiber was cemented onto the metal rod. After all assemblies were cemented, the ground wires were soldered together, and the individual connectors were molded into a single multichannel connector. An implantation-ready device weighed 0.5–1.5 g.

For constructing tetrode-based diode probes (Fig. 2*C*), each tetrode, made by twisting four 12-$\mu$m tungsten wires (California Fine Wire), was first placed into a silica tube (internal/external diameter: 76/153 $\mu$m; Polymicro). The tetrode was then attached (using UV glue under microscopic guidance) to a diode-coupled fiber such that the fiber tip was ~100 $\mu$m above the end of the tetrode (Fig. 2*C*, *right*) and the proximal (jacketed) end of the fiber was glued to the silica tube (resulting in a maximal diameter of 250+153 $\mu$m). After multiple diode-fiber-tetrode assemblies were ready, each was loaded into a standard multitetrode drive (Fig. 2*C*, *left*) that was modified in two ways: *1*) instead of 29-gauge tubes, the fixed part of the drive consisted of 23-gauge stainless-steel hypodermic tubes (internal diameter, 508 $\mu$m; Small Parts) that could freely accommodate the assemblies while supporting precise anatomic localization; and *2*) the moving part of the drive was supplemented with 10-mm, 28-gauge tubes onto which diode bodies were cemented. The rest of the process was the same as for a silicon diode-probe array.

*Multichannel Precision Current Source for Diode Driving*

Each diode was driven by a separate channel of a custom-built 16-channel linear current source. The current source was designed to enable independent and parallel driving of up to 16 loads with currents of up to 100 mA per channel. Thus grounded loads could be driven, simplifying wiring to the animal and enabling programming relative to ground. The device was driven by 15-V voltage regulators, yielding linear compliance for 0- to 5-V programming and output voltage drops of up to 10 V; this enabled driving high-forward voltage diodes such as blue LEDs and laser diodes. Digital [transistor-transistor logic (TTL)] inputs were translated to 5 V internally to enable driving loads with either digital or analog inputs; source selection was made by a toggle switch. The maximal current delivered by each channel was tuned using an external 1-k$\Omega$ potentiometer. The schematic for a single-channel driver is shown in Fig. 2*D*; for modularity, the actual device consisted of 4 identical custom-made 4-channel boards. To enable arbitrary mapping between analog inputs and loads (e.g., to drive multiple loads by the same waveform), a 16-channel all-to-all multiplexer board, controlled by dual inline package (DIP) switches, was constructed and placed before the individual boards. The end product was a 16-channel true current source, with linear compliance of up to 10-V voltage drop at the load, that could precisely follow inputs up to the 100-kHz range (<0.5-$\mu$s delay for a square-pulse input) and drive up to 16 simultaneous 100-mA loads with arbitrary waveforms.

In the digital mode, current was typically fixed (to 20–60 mA, depending on the diode), and the circuits were driven by an RP2.1 digital signal processor (DSP; Tucker-Davis Technologies) controlled by MATLAB (The MathWorks) via ActiveX. In the analog mode, circuits were driven by analog outputs of the DSP or a PCI-6129 card (National Instruments) controlled by the MATLAB data acquisition toolbox. A 12- or 40-strand lightweight wire (New England Wire Technologies) carried leads from each circuit to the diodes on the headstage. This configuration enabled driving any number of diodes, separately or simultaneously, at arbitrary waveforms, amplitudes, and times.

*Diode-Fiber Coupling: Theoretical Considerations*

For a uniform planar (Lambertian) light source of area $A_s$ and a straight (cleaved) optical fiber of cross-sectional area $A_f$ having a numerical aperture $NA_{in}$, the maximum coupling efficiency is (Hudson 1974) $\eta_{meridional} = P_f / P_s = A_f / A_s \cdot \sin^2\gamma$, where $\gamma$ is the acceptance angle of the fiber for meridional rays, $\sin\gamma = NA_{in}/n_{in}$, and $n_{in}$ is the RI of the medium outside the fiber (1 for air). In the case of a small fiber $A_f < A_s$, there is no gain by using collimating optics; the theoretical maximum can be achieved when the fiber is resting directly on the source providing there are no reflection losses (Saleh and Teich 2007). Thus an LED with emitter size 250 × 250 $\mu$m butt-coupled to a 50-$\mu$m diameter fiber with 0.22-NA via air has a maximal theoretical coupling efficiency of 0.15%. For the same fiber, a laser diode (a non-Lambertian source) with ~20° beam divergence and an emitter of 1 × 100 $\mu$m has two orders of magnitude higher theoretical maximum efficiency (20–30%).

Two factors, which have opposing practical implications, were ignored in the foregoing: *1*) reflective losses; and *2*) skew rays. Since there are inevitable differences between the RIs of the source, coupling medium, and fiber core, there is attenuation due to reflection at each interface. This is quantified by the Fresnel equations; for unpolarized light traveling from a source with RI of $n_s$ to a target $n_t$, the attenuation is $1 - (n_s - n_t)^2/(n_s + n_t)^2$ at each interface. For empirical RI values (e.g., diode die: 1.525; fiber core: 1.457; and air: 1), there is 8% loss due to reflections. Using a coupling interface with an index similar to the indices of the source and fiber ($n_{in} \approx n_{source} \approx n_{core}$; e.g., NOA-61, Norland Products; RI of 1.56/1.57 for red/blue light) reduces these reflective losses considerably (to <1%) but at a cost of reducing the effective acceptance angle $\gamma$ of the fiber by a factor of $(1/1.57)^2 = 41\%$. The above treatment applies to rays that cross the fiber axis (meridional rays), but circular fibers can also transmit rays, which propagate in a helical fashion in the fiber core (skew rays) as long as the angle they make with the fiber axis is smaller than $\theta = \sin^{-1}(n_{in}/n_{core})$. $\theta$ Is typically much larger than $\gamma$ (for the above fiber, the values are 12.7 and 43.6°), and thus a considerable part of noncollimated light accepted into a multimode fiber is from nonmeridional rays (Colvin 1974). Although not all rays falling within the $\theta$ cone will be transmitted (the exact fraction exhibits a complex dependency on $\gamma$, $n_0$, and the angle of the ray relative to the fiber axis; Potter 1961), the effect of applying an index-matching medium on the skew rays acceptance angle $\theta$ is diametrically opposite from that on acceptance angle of meridional rays, $\gamma$. For instance, applying a coupling medium with an index higher than the core index (e.g., 1.57) enables acceptance of skew rays from all directions, yielding a twofold increase in the coupling efficiency (see below). These considerations indicate that substantial improvement in coupling efficiency can be obtained even for noncollimated sources by using an index-matching medium.

In sum, coupling is more efficient when the source has small area, when the fiber has a large diameter and high NA, when the source and fiber are placed in close proximity, and when reflective losses are

minimized and skew ray transmission is maximized by using a source, medium, and fiber with as similar RIs as possible.

### *Power-Intensity Transformation: Design Equations*

The overall transformation from light power at the source $P_s$ (milliwatts) to light intensity I (milliwatts per square millimeter) at a distance $d$ (millimeters) from the fiber tip in brain tissue can be estimated as

$$\mathrm{I} = P_s \cdot \eta_{coupling} \cdot \eta_{scatter} \cdot \Phi_{geometry} \qquad (1)$$

where $\Phi_{geometry}$, the geometric dispersion, is 1/mm$^2$. Briefly, for a Lambertian source with $A_s$ coupled to a fiber with a radius $r_0$ and a $NA_{in}$ via a medium with a RI $n_{in}$, the maximal coupling efficiency is $\eta_{coupling} = \pi r_0^2/A_s \cdot (NA_{in}/n_{in})^2 \cdot c$, where $c$ is an empirical correction factor for Fresnel and skew rays compensation ($c \approx 2n_{in}^2$). In brain tissue, for $d < 1$ mm, a $1/d$ scattering model (Aravanis et al. 2007) provided a good approximation to the power attenuation, so $\eta_{scatter} = 1/[s(\lambda) \cdot d + 1]$, where $s(\lambda)$ is the scattering coefficient for wavelength $\lambda$ (Fig. 3 and APPENDIX). Finally, for any $r \leq r_0 + d\tan[\sin^{-1}(NA_{out}/n_{out})]$, the geometric attenuation could be approximated by $\Phi(r,d) = 1/\pi\{r_0 + d\tan[\sin^{-1}(NA_{out}/n_{out})]\}^2$. Thus the final expression for the approximate I obtained by coupling a Lambertian source to an etched optical fiber as a function of distance from the fiber tip $d$ is

$$\mathrm{I}(d) = \frac{P_s \cdot 2r_0^2 NA_{in}^2}{As \cdot [s(\lambda)d + 1]\{r_0 + d\tan[\sin^{-1}(NA_{out}/n_{out})]\}^2} \qquad (2)$$

where $n_{out}$ is the RI of the output medium (brain).

### *Animal Procedures*

All animal handling procedures were approved by the Rutgers University Animal Care and Facilities Committee. Rats (Long-Evans, male, 300–500 g) were trained to run in the dark on an elevated 8 × 150-cm linear track for liquid reward. The track was equipped with 2 water-delivery solenoids (Parker) and 3 infrared position sensors (Omron), 1 next to each water port and 1 portable. Water (0.05 ml) was delivered to 1 port when the animal crossed the beam of the nearby sensor after crossing the distant sensor, enabling a fully automated control of the task (PCI-6221 and LabVIEW; National Instruments). Animals ran ~100 laps in a single session; the average lap duration was 3.5 ± 1 s (mean ± SD).

Adeno-associated viruses (AAV; rAAV2/5 CAG-ChR2-tdTomato) were obtained from Dr. Karel Svoboda (Janelia Farm Research Campus, Howard Hughes Medical Institute) and from the University of North Carolina viral core facility (rAAV5 CAG-ChR2-GFP, courtesy of Dr. Ed Boyden; rAAV5 CaMKII-eNPHR3.0-EYFP, courtesy of Dr. Karl Deisseroth; Gradinaru et al. 2010), with titers estimated at

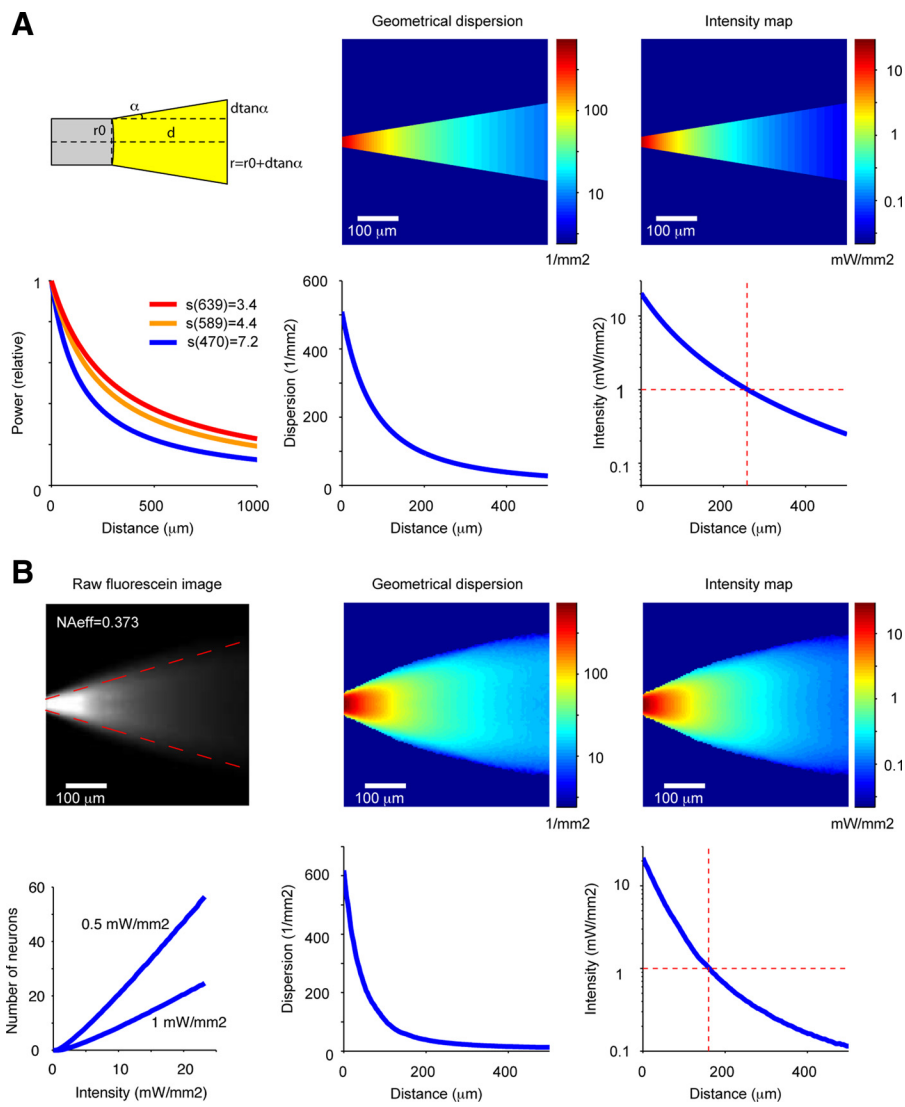


Fig. 3. Estimation of light intensity in brain tissue. *A*: theoretical calculation for an idealized cleaved fiber. *Top left*: scheme of the geometric arrangement; gray, cleaved fiber; yellow, idealized light cone [0.22-numerical aperture (NA) fiber, resulting in divergence angle ($\alpha$) = 9.3° in brain tissue]. *Bottom left*: light attenuation through brain as a function of wavelength (470, 589, and 639 nm) and the thickness of brain tissue between the fiber tip (inserted into a piece of brain) and the measurement sensor (placed just below the brain). *Middle*: geometric dispersion of light (the inverse of the cone cross-section) as a function of the distance ($d$) and the radius ($r$) from the fiber tip (*top*) and along the optical axis (fiber center; *bottom*). *Right*: light-intensity map (source: blue light, 40 $\mu$W at tip of fiber) in the same coordinates as the geometric dispersion map; vertical dashed red line shows the distance for which intensity falls below threshold (1 mW/mm$^2$). *B*: empirical calculation for a pointed fiber. *Top left*: fluorescence image of the cone of blue light emitted by a 0.22-NA fiber etched to a point (viewed via an FITC filter). The measured divergence in PBS (0.1 M) is $\alpha$ = 16.3°, resulting in an effective NA (NAeff) of ~0.37. *Middle*: geometric dispersion map, estimated from the fluorescence image. Note that the distribution of light is not uniform at locations equidistant from the source and that the distance attenuation is stronger than for a cleaved fiber. *Right*: blue light intensity map for this fiber. *Bottom left*: number of neurons in illuminated brain tissue as a function of blue light intensity at the fiber tip. The estimation, shown for 2 different intensity thresholds for ChR2 activation, assumes neuronal density of 20,000 cells/mm$^3$ and ignores shadowing by the probe shank.

$\sim 10^{12}$ IU/ml. Small amounts of viral solutions (55 nl) were injected into multiple sites in the wild-type rat brain using a volume-based microinjector (Nanoject II; Drummond) mounted on a stereotactic frame (Kopf). For targeting the rat hippocampus, three 0.2-mm holes were made at PA $-3.3 \pm 0.5$ and ML $3.0 \pm 0.5$, and virus was injected at 0.2-mm intervals (CA1: DV $2.2 \pm 0.2$; dentate gyrus: $2.9 \pm 0.2$; CA3: $3.3 \pm 0.2$) for a total of nine injection sites per structure. Somatosensory cortex was targeted at DV $1.5 \pm 0.2$. Following the injections, the scalp was sutured, and rats were allowed to recover for at least 2 wk. For experiments with freely moving mice, male mice heterozygous for a loxP-ChR2 conditional allele [Rosa-CAG-LSL-ChR2(H134R)-EYFP-WPRE; Ai-32; Allen Institute] were cross-bred with homozygous females expressing Cre recombinase under the control of the CaMKII$\alpha$ (CaMKII) or parvalbumin (PV) promoter [B6.Cg-Tg(Camk2a-cre)T29-1Stl/J and B6;129P2-Pvalb tm1(cre)Arbr/J; The Jackson Laboratory].

Probes were implanted following previously described methods (Fujisawa et al. 2008). Briefly, under isoflurane anesthesia, after preparing the skin for surgery and making a midsagittal cut, the skull was cleaned, and multiple screws (000-120x1/16; Small Parts) were implanted in the skull along the lateral crests. Two screws, inserted above the cerebellum, served as ground and reference (Fig. 1*D*). Although the bone typically healed within 2–3 wk, injection sites were easily recognized even 2 mo after injection by small dents and confirmed by stereotactic measurements. After dental cement (Metabond; Parkell) was applied to the periphery of the skull, a craniotomy was made, and the dura mater was excised. Next, the diode probe, connected to a microdrive, was inserted to a depth of $\sim$1 mm above the target site, and silicon mixture (3-4680; Dow Corning) was applied around the shanks to cover the brain and prevent infection. Finally, a copper mesh cage was built around the probe for mechanical and electromagnetic shielding, and the recording and stimulating connectors were cemented to inside of the mesh wall. Animals were treated with postoperative antibiotics (7.5 mg/kg; Enrofloxacin) and analgesics (0.05 mg/kg; Buprenorphine) and allowed to recover for 7 days during which diode probes were gradually moved to the target area.

### *Electrophysiology, Real-Time Signal Processing, and Data Analysis*

At each site, neuronal activity was examined for spiking and optical responses. Neural activity was filtered (1–5,000 Hz), amplified (20$\times$ by Plexon headstages and 50$\times$ by an RC Electronics system), and digitized (20 kHz) on a 128-channel DataMax system (RC Electronics). Signals from up to 4 channels were further band-pass filtered (300–6,000 Hz) and amplified (20$\times$), and spikes were detected online using amplitude-based windowing (0.15-ms delay; NeuroLog; Digitimer) or detected and sorted using template matching hardware (2.6-ms delay; ASD; Alpha Omega). In other experiments, signals were processed online using a programmable DSP (RP2.1; TDT) to detect $\theta$ (5–11 Hz) activity, power, and phase in real time. These digitized signals were used, sometimes in conjunction with behavioral data (crossing of infrared sensors), to trigger closed-loop diode activation in predetermined spatiotemporal patterns. The animal's position was recorded from above using a charge-coupled device (CCD) camera synchronized to the recording DataMax system, monitoring the position of 2 LEDs located $\sim$8 cm apart, 1 on each side of the headstage. The video signal was digitized and recorded on 1 computer; all other signals were recorded by the DataMax system.

Offline, spikes were detected in the wideband (1–5,000 Hz) signals, and the waveforms were projected onto a common basis obtained by principal component analysis (PCA) of the data and sorted into single units automatically (Harris et al. 2000) followed by manual adjustment. Units were required to fulfill the following criteria: *1*) amplitude: peak-to-peak amplitude $>50$ $\mu$V; *2*) morphological isolation: $L_{ratio}$ (Schmitzer-Torbert et al. 2005) below 0.05; and *3*) temporal isolation: interspike-interval histogram with a clear refractory period (count in the 1st 2 ms below 0.2 of the expected count given the counts in the 1st 20 ms; Fee et al. 1996). A total of 535 hippocampal and 98 neocortical units conformed to these criteria. To be included in statistical analyses (Figs. 4–6), units were required to fire at least 100 spikes at a baseline rate $>0.01$ spikes/s; this yielded a data set of 135/72 hippocampal units (rat/mouse) and 39 neocortical units (rat). Units were classified as putative excitatory or inhibitory cells based on short-latency features in cross-correlation histograms (Fujisawa et al. 2008).

To determine the effect of light on spiking, spike trains were binned into 1-ms bins, and raster and peristimulus time histograms (PSTHs) were constructed around stimulus onset. Stimulus period was defined as the time light was on and baseline as the period subtending two stimulus periods that began three stimulus periods before light onset. From these data, the following parameters were determined.

*Firing rate during light.* This was the mean number of spikes per bin during the stimulus period divided by number of stimuli and bin size. Baseline rate: same, for the baseline period.

*Light-modulated units.* These were neurons with a low ($<0.05$) $P$ value on a Mann-Whitney $U$ test comparing, over all stimulation trials, the median number of spikes per bin during the stimulus and baseline periods.

*Spiking probability (conditioned on photostimulus).* This was defined as the number of trials with at least one spike during the stimulus period divided by the total number of light stimuli. Randomized probability: same, for randomly selected stimulus onset times.

*Waveform consistency.* For each unit, each spike waveform was recorded on multiple (4–10) sites of the multielectrode array and projected onto a common basis (obtained by the PCA of the data) consisting of 3 eigenvectors per site for a total of up to 30 coefficients. These coefficients were then averaged over all spikes that occurred during light stimulation to arrive at a mean waveform description vector. The same was repeated for all spikes that occurred during spontaneous activity. The 2 vectors were then correlated, yielding a measure (range, $-1$ to 1) of the consistency of the waveform during light stimulation and spontaneous activity. Statistical significance of the consistency was assessed by randomly permuting the labels of spikes (light and spontaneous) and repeating the correlation-coefficient computation.

*Latency.* This was the time (relative to stimulus onset) of first PSTH bin that was significantly different from baseline. Significance was determined by the Poisson distribution with a Bonferroni correction for the number of bins in the stimulus period.

*Center-of-mass.* For a given spike train, the center-of-mass is defined as the mean spike time relative to an arbitrary temporal reference. The center-of-mass of spike times (relative to stimulus onset) in significantly high PSTH bins was computed for each trial and averaged over all stimulation trials with at least one spike during the stimulus period. Significant bins were determined from the PSTH as for the latency calculation.

*Precision.* This was the standard deviation (across trials) of the trial-to-trial centers-of-mass.

### *Histology*

Following completion of electrophysiological experiments, electrolytic lesions were made at two to three sites per shank (5-$\mu$A anodal current for 10 s; Fig. 1*D*, *inset*, arrow). Twenty-four hours later, the animals were perfused through the heart with 0.9% NaCl followed by 4% paraformaldehyde. The brains were removed, postfixed in paraformaldehyde for 24 h, and kept in 0.1 M PBS, and 80-$\mu$m sections were cut by a microtome (Leica). Odd sections were stained for Nissl substance, and even sections were mounted on a slide, covered with a protective medium (Vectashield H1400; Vector Laboratories), and coverslipped. Sections were subsequently viewed and photographed (Zeiss) under light (Nissl) and fluorescence microscopy (BH2; Olympus).

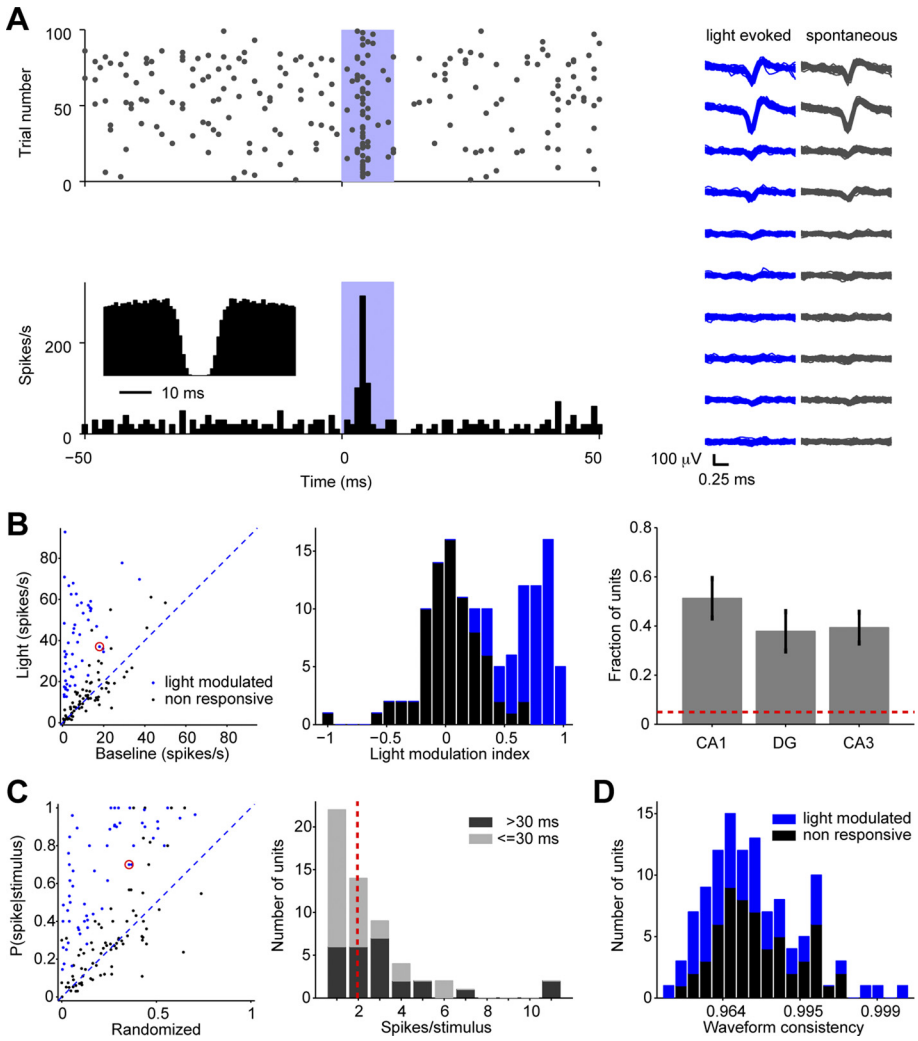


Fig. 4. Diode probe induction of neuronal activity in the freely moving wild-type rat. *A*: example of the effect of low intensity light on the activity of a single unit in the rat hippocampus (dorsal CA1). Raster plot (*top*) and peristimulus time histogram (PSTH; *bottom*) of spiking activity during 100 light stimuli, each 10 ms long (blue bar; 4 $\mu$W at fiber tip, corresponding to ~0.12 mW/mm$^2$ at the shank center). *Inset* shows autocorrelation histogram. *Right*: wideband (1–5,000 Hz) spike waveforms. *B*: effect of localized light on spiking rate. *Left*: firing rates during light vs. spontaneous activity. Red circle marks unit shown in *A*. *Middle*: light modulation index (difference between firing rates during photostimulation and baseline divided by the sum). The distribution is bimodal. *Right*: fraction of light-modulated units is above chance level (dashed red line) and does not differ between CA1, dentate gyrus, and CA3 regions of the hippocampus. *C*: effect of light on spiking probability. *Left*: spiking probability during light vs. during spontaneous activity. Conventions are the same as in *B*. *Right*: number of spikes per light stimulus. Stimuli were rectangular light pulses, 2–50 ms long; units are partitioned according to the median pulse duration used (30 ms). Dashed red line shows median number of spikes per stimulus (1.92). *D*: effect of light on extracellular waveform. Waveform consistency was defined as the Pearson correlation between the mean waveforms during light and during spontaneous activity.

## RESULTS

### *Diode-Probe Construction and Stimulation Efficiency*

To enable multisite photostimulation and neuronal recordings, we coupled miniature diodes to small-core (50 $\mu$m) multimode optical fibers and integrated them with multishank silicon probes (Fig. 1) and multitetrode arrays (Fig. 2). Low-current (5–60 mA) driving of blue LEDs resulted in light output of up to 40 $\mu$W at the fiber end. The volume of the illuminated brain tissue [at an intensity of >1 mW/mm$^2$, the documented threshold for stimulating channelrhodopsin2 (ChR2); Aravanis et al. 2007; Boyden et al. 2005] was ~0.001 mm$^3$, formed by a truncated cone with 180-$\mu$m height and 150-$\mu$m base diameter (Figs. 1*B* and 3). Red laser diodes driven by similar currents yielded ~180 $\mu$W at the fiber tip and subtended a similar volume [at an intensity of >7 mW/mm$^2$, a level sufficient for stimulating halorhodopsin eNpHR3.0 (Halo) with red light; Gradinaru et al. 2010]. Assuming neuronal density of 20,000–100,000 cells/mm$^3$ (Braitenberg and Schüz 1998; West et al. 1991), the illuminated volume contained an estimated number of 20–100 cells, many of which can be monitored by a multisite shank of a silicon probe (Buzsáki 2004). The number of illuminated neurons, which is in direct proportion to light intensity at the fiber tip (Fig. 3*B*, *bottom left*), could be controlled by varying the diode current.

To test the in vivo effect of the diode probes, multiple diode-coupled fibers were attached to a multishank silicon probe or a multitetrode array mounted on a movable drive, one assembly per shank (Fig. 1*C*). The resulting optoelectronic arrays were implanted in the brains of wild-type rats (expressing exogenous opsins CAG-ChR2 and/or CaMKII-Halo; Fig. 1*D*) and transgenic mice (expressing ChR2 under the control of a CaMKII or PV promoter). When placed in the hippocampus of freely moving rats expressing ChR2, stimulation with rectangular pulses of weak blue light (3–30 $\mu$W at the fiber tip; 0.1–1 mW/mm$^2$ at the shank center) evoked reliable spiking at high temporal precision (Fig. 4*A*, *left*) without distorting spike waveforms (permutation test, $P = 0.12$; Fig. 4*A*, *right*). A considerable fraction of the tested units (42%; 57/135 units, recorded by 13 shanks in 4 rats) modulated their firing rates during blue light stimulation (Mann-Whitney *U* test, $P < 0.05$; Fig. 4*B*, *left*). This relatively high fraction of light-modulated units may be due to the high ChR2 transduction rates typically obtained with AAV vehicles (40–80%; Cardin et al. 2010; Diester et al. 2011) and the proximity of the fiber tip to the recording sites (≥50 $\mu$m). Although the definition of light-modulated spiking was statistical, light modulation indices (difference between firing rates during photostimulation and baseline divided by the sum) exhibited a bimodal distribution (medians for nonresponsive/light-modulated units, 0.045/0.76;

*U* test, $P < 0.001$; Fig. 4*B*, *middle*). The probability to encounter light-modulated units did not depend on the tested brain region (hippocampal regions CA1, dentate gyrus, and CA3: 0.51/0.38/0.39; $\chi^2$-test, $P = 0.7$; Fig. 4*B*, *right*), indicating the general applicability of the approach.

Spiking probability during blue light stimulation was considerably higher than during duration-matched periods (median ratio, 1.82; Wilcoxon paired signed-rank test, $P < 0.001$; Fig. 4*C*, *left*). For light-modulated units, the median spiking probability during a photostimulus was 0.7, and effective stimuli typically evoked one or two spikes (median 1.3/2.5 spikes per stimulus for stimulus durations below/above 30 ms; *U* test, $P = 0.003$; Fig. 4*C*, *right*). Spikes could be recorded by all sites of the silicon probe including sites close to the optical fiber tips (e.g., Fig. 4*A*, *right*), indicating that the additional volume of the fiber did not cause significant local ischemia or neuronal damage. Moreover, extracellular spikes were not superimposed and distorted by the weak light pulses (Royer et al. 2010), as spike waveforms during light and during spontaneous activity were similar (median waveform consistencies for light-modulated/nonresponsive units: 0.977/0.983; *U* test, $P = 0.19$; Fig. 4*D*).

### *Temporal and Spatial Resolution of Diode-Probe Photostimulation*

The temporal relations between light stimulation and spiking were quantified by two correlated measures: spiking center-of-mass (median, 12 ms; $n = 57$ light-modulated units; Fig. 5*A*, *left*) and latency (median, 5.5 ms; Fig. 5*A*, *center*). Latencies

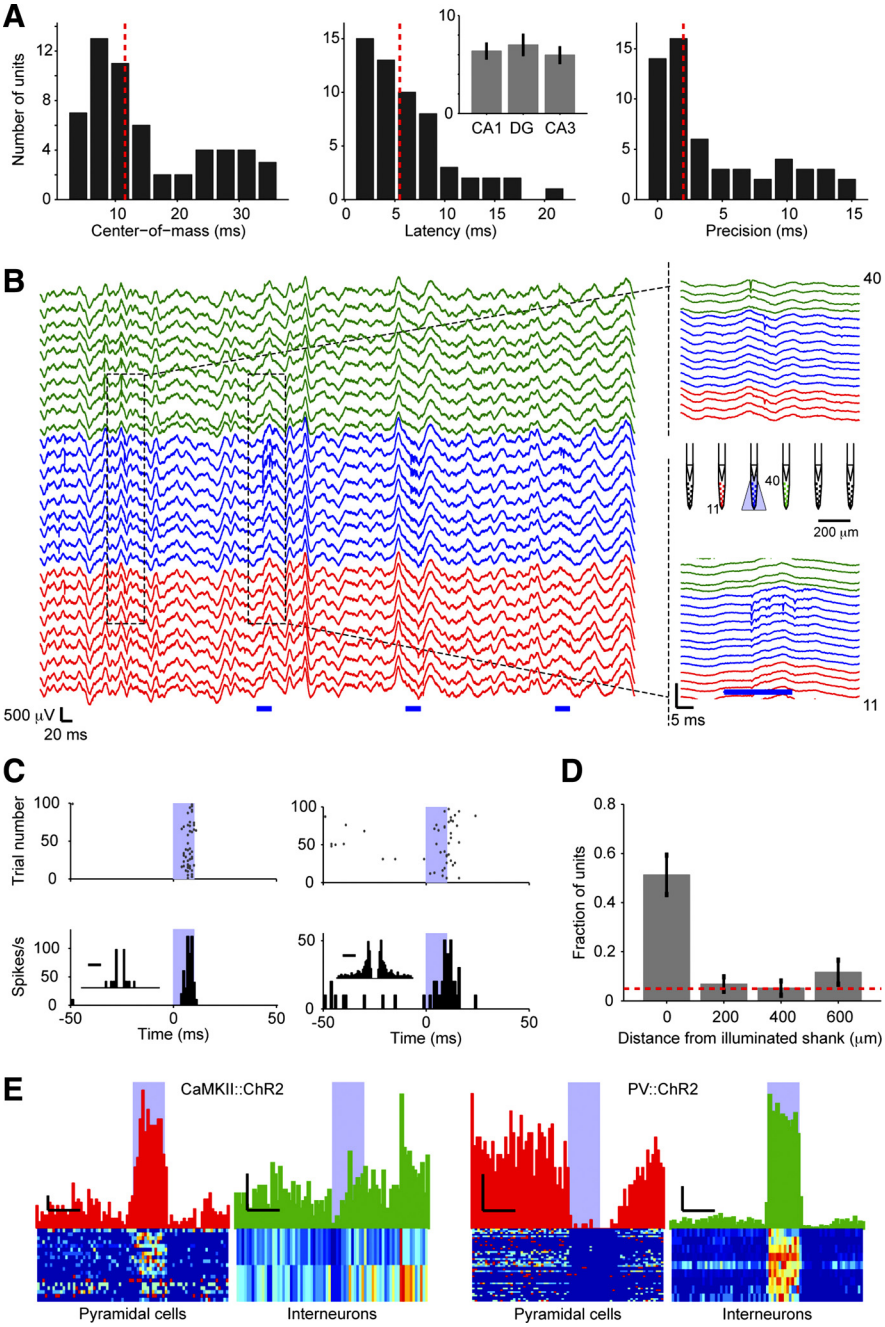


Fig. 5. Spatiotemporal extent of diode-probe light stimulation. *A*: temporal precision of light-induced spiking. *Left*: spiking center-of-mass relative to stimulus onset (across-trial average of trial-specific centers-of-mass). Dashed red line, median. *Middle*: spiking latency (time to 1st significantly high PSTH bin). *Right*: spiking precision (across-trial SD of the trial-specific centers-of-mass). *B*: example of spatially localized light-induced spiking. Wideband (1–5,000 Hz) traces during light stimulation. Red/blue/green traces show recordings from channels 11 through 40 (*shanks 2–4*) of a 6-shank silicon probe implanted in the dorsal CA3 pyramidal layer of the rat hippocampus. Probe geometry is shown at *right*; blue light was applied locally at *shank 3* (blue bars; 20-ms pulses, 5 Hz, 0.15 mW/mm$^2$ at shank center). *Top right*: expanded view during spontaneous activity, showing spiking on 3 adjacent shanks. *Bottom right*: expanded view during shank-specific light stimulation, showing light-driven spiking specifically on the illuminated shank. Note lack of electromagnetic or light artifacts. *C*: 2 light-responsive single units recorded on *shank 3*. Conventions are the same as in Fig. 4*A*. *D*: spatial extent of the localized light stimulus (CA1 pyramidal layer; 10 shanks in 3 rats). In contrast to the illuminated shank, the fraction of light-modulated units on other shanks does not differ significantly from chance level (exact binomial test, $P > 0.05$; dashed red line corresponds to 0.05, the fraction of units expected to be defined as modulated assuming that the null hypothesis of "no light modulation" is correct). Error bars, SE. *E*: cell type-specific stimulation in freely moving mice (CA1). *Bottom*: each row corresponds to the 4-ms binned PSTH of 1 unit, averaged over 60 light pulses, and scaled to 0–1. *Top*: before scaling, all PSTHs were averaged; horizontal calibration: 50 ms; vertical calibration: pyramidal cells, 1 spike/s; interneurons: 20 spikes/s. During stimulation (~0.9 mW/mm$^2$), putative pyramidal cells are activated in CaMKII::ChR2 and silenced in PV::ChR2 mice.

were similar for units recorded in different regions of the hippocampus (CA1, dentate gyrus, and CA3; median latencies: 6/6.5/5 ms; Kruskal-Wallis test, $P = 0.61$; Fig. 5*A*, *inset*). Finally, the temporal precision of light-evoked spiking, quantified by the across-trial standard deviation of the centers-of-mass, was in the millisecond range (median, 2 ms; Fig. 5*A*, *right*), indicating that weak blue light could yield precise temporal control of concurrently recorded units.

Illumination of only one shank of a silicon probe typically resulted in spiking of several units in the same locality (Fig. 5*B*, blue traces; Fig. 5*C* shows spiking statistics for two units isolated from the illuminated shank). The weak (<40 $\mu$W) light stimulus did not result in local field potential (LFP) artifacts (Figs. 5*B*, 6*A*, 7*A*, and 8*A*) as often seen when light power several orders of magnitude higher is used (1–10 mW; Cardin et al. 2010; Han et al. 2009; Kravitz et al. 2010). To quantify the spatial extent of light-induced spiking, we used recordings from region CA1 of the hippocampus, where neurons have relatively few recurrent excitatory connections (Thomson and Radpour 1991). Fixing light intensity to 0.1–0.2 mW/mm$^2$ at the shank center, we found that whereas units recorded on the illuminated shank were often modulated (10 shanks in 3 rats; 20/39 units; 52%), the fraction of modulated units on other shanks (≥200 $\mu$m away) was at chance level (nearby shank: 5/73, 6.8%; exact binomial test, $P > 0.05$ for units recorded on any nonilluminated shank; Fig. 5*D*). Thus the multidiode/-electrode array configuration enables not only temporally precise, but also spatial control in a small volume of intact brain, which can be monitored simultaneously by the recording electrodes.

Circuit analysis in small behaving animals can be facilitated by diode probes. For that purpose, we implanted mice with 4-shank diode probes and sorted units into putative excitatory and inhibitory cells based on cross-correlation patterns in the absence of light stimulation. When placed in the CA1 region of CaMKII::ChR2 mice, blue light stimulation (50 ms, ~0.9 mW/mm$^2$ at the shank center) resulted in robust spiking of putative pyramidal cells but not of interneurons (Fig. 5*E*, *left*). In contrast, blue light stimulation with identical parameters in the CA1 of PV::ChR2 mice resulted in robust spiking of interneurons followed by silencing of nearby pyramidal cells (Fig. 5*E*, *right*). Thus diode probes enable spatiotemporal control of specific cell types in various species.

### *Concurrent Neuronal Activation and Silencing in Freely Moving Animals*

Diode probes can also provide multicolor photostimuli under independent time control for each color, thereby allowing precise temporal manipulation of spike timing in freely moving animals. To illustrate this, we combined blue and red light stimulation on adjacent shanks of diode probes implanted in wild-type rats expressing both CAG-ChR2 and CaMKII-Halo. Relatively strong red light pulses (200 ms, 220 $\mu$W at the fiber tip, corresponding to 9.2 mW/mm$^2$ at the center of the illuminated shank), given on *shank 2* of a six-shank diode probe, were occasionally paired with two blue light pulses on *shank 1* (10 ms, 11 $\mu$W; 0.35 mW/mm$^2$ on shank center; Fig. 6*A*). This resulted in reliable activation of units on *shank 1* during blue light pulses and robust silencing of the same units during the red light pulses (Fig. 6*B*, *left* and *right*). Moreover, brief blue light pulses delivered during red light stimulation resulted in consistent (spiking probability, 0.7) activation of the silenced neurons (Fig. 6*B*, *middle*), albeit with a longer latency supposedly due to the red light-induced hyperpolarization of the membrane. Notably, the ability of ChR2-induced depolarization to overcome the halo-induced hyperpolarization depended sharply on blue light intensity: 70% of the 0.35 mW/mm$^2$ blue-light pulses but only 10% of 0.28 mW/mm$^2$ pulses were efficient ($\chi^2$-test, $P < 0.01$). Thus diode probes enable activation and silencing of the same neurons in freely behaving animals.

Since the intensity of light emitted by the laser diode-coupled fibers could be modulated to a wider range than the LED-coupled fibers, we explored the relation between light intensity, effect size, and the spatial extent of light modulation. Although a rate decrease was already evident at intensities of ~5.5 mW/mm$^2$ (shank center), spiking activity recorded by the illuminated shank was typically not completely abolished at such intensities (Fig. 6*C*). Although the fraction of significantly light-modulated units exhibited a marked increase between 3.5 and 5.5 mW/mm$^2$ (from 15 to 73%), the light modulation index increased monotonously with light intensity up to 13.7 mW/mm$^2$ and then saturated at near-complete silencing ($-0.9 \pm 0.034$, mean ± SE; 18 units, recorded on 2 red-illuminated shanks; Fig. 6*D*, *top*). Units recorded on nonilluminated shanks were modulated to a lesser extent than on the illuminated shank: whereas on the illuminated shanks intensities ≥5.5 mW/mm$^2$ resulted in above-chance silencing, 400 $\mu$m away from the illuminated shank units were affected only at intensities >7.1 mW/mm$^2$ (light measured on the center of the illuminated shank) and units 600 $\mu$m away were affected from intensities only >15.2 mW/mm$^2$ (39 units, recorded on 6 shanks; exact binomial tests, $P < 0.05$ in all cases; Fig. 6*D*, *bottom left*). Even at the highest intensities, the effect of red light on units recorded 400 $\mu$m from the illuminated shank was comparable with the local effect at threshold intensity ($-0.48 \pm 0.11$ on the local shank at 5.5 mW/mm$^2$ vs. $-0.42 \pm 0.04$ 2 shanks away at 16.7 mW/mm$^2$; mean ± SE; *U* test, $P = 0.58$), whereas the effect on units 600 $\mu$m was yet lower ($-0.1 \pm 0.05$ at 18.2 mW/mm$^2$; *U* test, $P = 0.01$; Fig. 6*D*, *bottom right*). These results illustrate that, presumably due to the larger spatial spread of red light (relative to blue; Figs. 1*B* and 3*A*) and the high coupling efficiencies of laser diodes (relative to LEDs), both localized and widespread optical modulation can be achieved with laser-based diode probes.

### *Closed-Loop Sequential Activation of Neurons in Behaving Animals*

The diode probes can deliver localized light at times triggered by ongoing behavioral or physiological parameters (closed-loop control), thereby allowing unique spatiotemporal activity patterns to be generated and observed in the intact brain. To demonstrate physiological closed-loop control in a freely moving animal, we used the activity of a well-isolated neuron recorded on one shank of a diode probe implanted in the CA1 pyramidal layer to trigger optical stimulation on multiple other shanks (Fig. 7*A*). Comparison of the cross-correlation histograms during illumination (Fig. 7*B*) and during baseline (Fig. 7*C*) shows that this manipulation resulted in transient modification of cross-correlation patterns in the net-

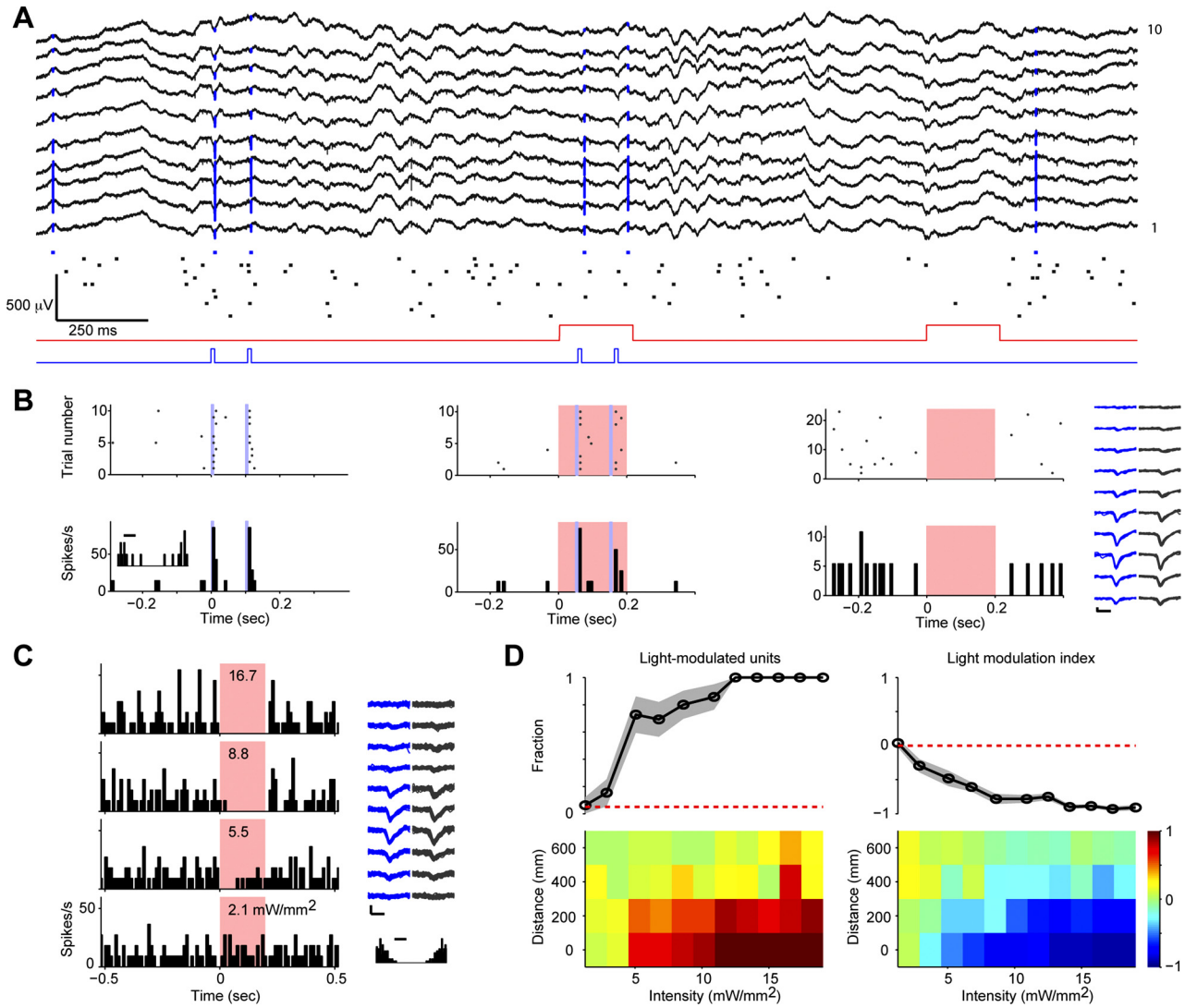


Fig. 6. Concurrent silencing and activation of the same neurons in the freely moving rat. *A*: multiple-unit example. Wideband (1–5,000 Hz) traces are from *shank 1* of a 6-shank multicolor diode probe implanted in layers 4 and 5 of the somatosensory cortex of a wild-type rat expressing CAG-ChR2 and CaMKII-Halo locally. *Bottom* traces show the occurrence of blue (10 ms, 0.34 mW/mm$^2$ on the center of the illuminated shank) and red (200 ms, 9.2 mW/mm$^2$) light pulses, delivered on *shanks 1* and *2*, respectively. Each row in the raster plot represents the spiking activity of 1 unit isolated from *shank 1*. Multiple units are activated (silenced) during the blue (red) light pulses. *B*: example statistics for 1 unit. Each PSTH-raster pair shows spiking activity of the unit marked in blue in *A* during blue light pulses (*left*), red light pulses (*right*), and concurrent red and blue light (*middle*). The unit is activated by blue light and silenced by red light; induced spiking is delayed during concurrent activation and silencing. *C*: example of unit silencing at multiple intensities. Effect of 200-ms pulses (1 Hz for 10 s) at varying intensities (2.1–16.7 mW/mm$^2$, measured at the shank center). *D*, *top left*: fraction of light-modulated units recorded on the illuminated shanks (dashed red line, $P = 0.05$). *Top right*: light-modulation index for the same units: 0, no effect; −1, complete silencing. Error bands, SE. *Bottom*: the probability of observing suppressed units and the light-modulation index depend on light intensity and on the transverse distance from the illuminated shank.

work and illustrates that diode probes can be used to study plasticity mechanisms in vivo.

For closed-loop control in behaving animals, rats were trained to run back and forth on a linear track for water reward. On 25% of the runs (alternating left-to-right trials), as the animal entered a predetermined part of the environment, we generated a sequence of photostimuli on multiple shanks (3–6 $\mu$W blue light, corresponding to 0.1–0.2 mW/mm$^2$ on the shank centers). For each shank, stimulus waveform was a single cycle of a modified sine wave, 1 s long, given on two different shanks with partial overlap (300-ms delay between stimulus onsets; Fig. 8*A*). This waveform was used instead of the rectangular pulses used in all other experiments to mimic the graded position-related spiking present during exploration in hippocampal activity (O'Keefe and Nadel 1978). Pyramidal cells recorded on the illuminated shanks often fired robustly during the photostimulus, yielding position-related spiking activity as a direct (light-evoked; Fig. 8*B*, *left*) and in some cases also an induced (internally generated; Fig. 8*B*, *right*, arrow) effect of the experimental manipulation. Despite the fact that the photostimuli were nonperiodic, some units exhibited $\theta$-frequency modulation of spiking during the stimulus (Fig. 8*C*, *top*), indicating interactions between light-induced and native-network control. Moreover, these units exhibited phase precession (O'Keefe and Recce 1993; slopes of circular-linear fit: 0.4 and 1.2°/cm; permutation test: $P < 0.01$ and $P < 0.05$; Fig. 8*C*, *bottom*), indicating that native network dynamics can incorporate synthetic patterns of activity. Thus spatially

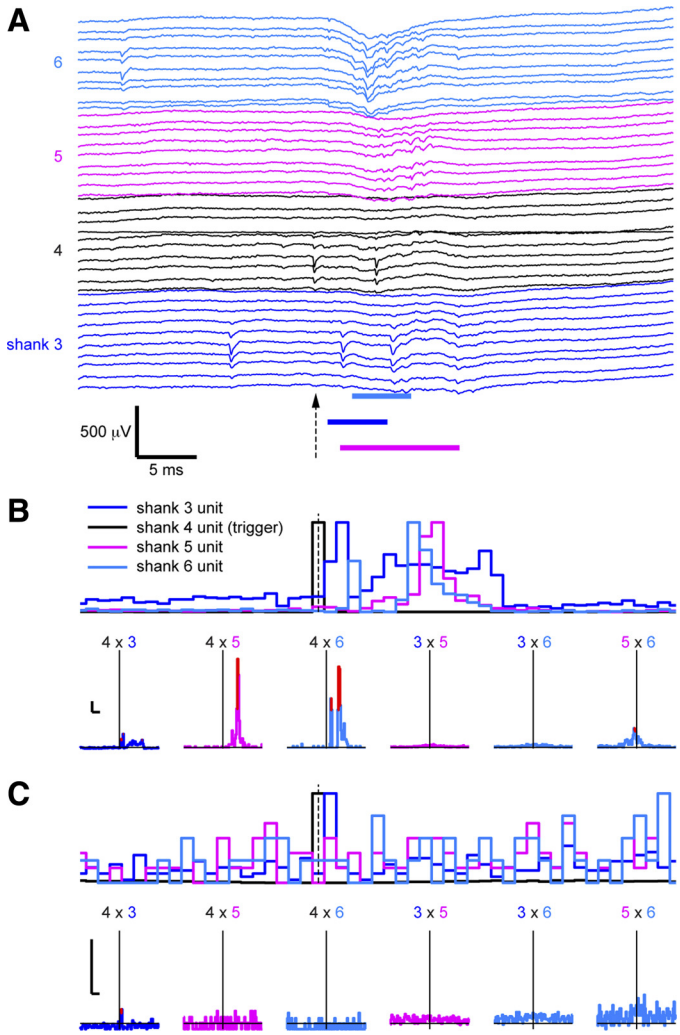


Fig. 7. Spike-triggered closed-loop spatiotemporal photostimulation in the freely moving animal. *A*: the plot shows a single 50-ms sweep through the recording. A spike was detected (arrow) and isolated in real-time from the wideband signal (1–5,000 Hz) recorded from *shank 4* of a 6-shank silicon probe implanted in dorsal CA1 of a wild-type rat injected with CAG-ChR2. One millisecond later, an arbitrary sequence of 3 blue light pulses (at the times indicated by the colored bars below the wideband traces) was given on *shanks 3*, *5*, and *6*. *B*: this resulted in consistent unit spiking, as evident by the multiunit PSTH (the spiking of each well-isolated unit was binned at 1 ms and normalized to the 0–1 range; *top*; same time scale as in *A*) and the cross-correlation histograms (CCHs) between the triggering pyramidal unit and 3 units on the other shanks (3 *bottom left* panels). CCHs were estimated in 0.5-ms bins and scaled to multiples of chance coincidence counts. Calibration for CCHs: horizontal, 50 ms; vertical, 10. Red-colored bins indicate significantly high counts (convolution method, window size, 10.5 ms). *C*: the same display as *B* but during a duration-matched (16 min) baseline period. Note that the precise temporal correlations in *B* were generated by the photostimuli, as CCHs between the same units were nearly flat (with an exception of a 1-ms lag between the units recorded on *shanks 4* and *3*) before the stimulation.

localized photostimulation can be used to probe the mechanisms of naturally generated network activity.

To demonstrate that arbitrary spatiotemporal firing patterns can be generated in a physiologically relevant manner in the behaving animal, the phase of the $\theta$-field potential oscillations (band pass, 5–11 Hz) was determined in real time. Once the animal reached a predetermined position, a train of stimuli, consisting of a sequence of brief (5 ms) rectangular light pulses on six shanks, was given on each $\theta$-cycle on a predetermined phase (e.g., trough) for a total of seven to eight consecutive cycles (1 s; Fig. 9*A*). This resulted in spiking of multiple units, one shank at a time, all within the same $\theta$-cycle, at a millisecond resolution (Fig. 9*B*). Stimulation was limited to a specific

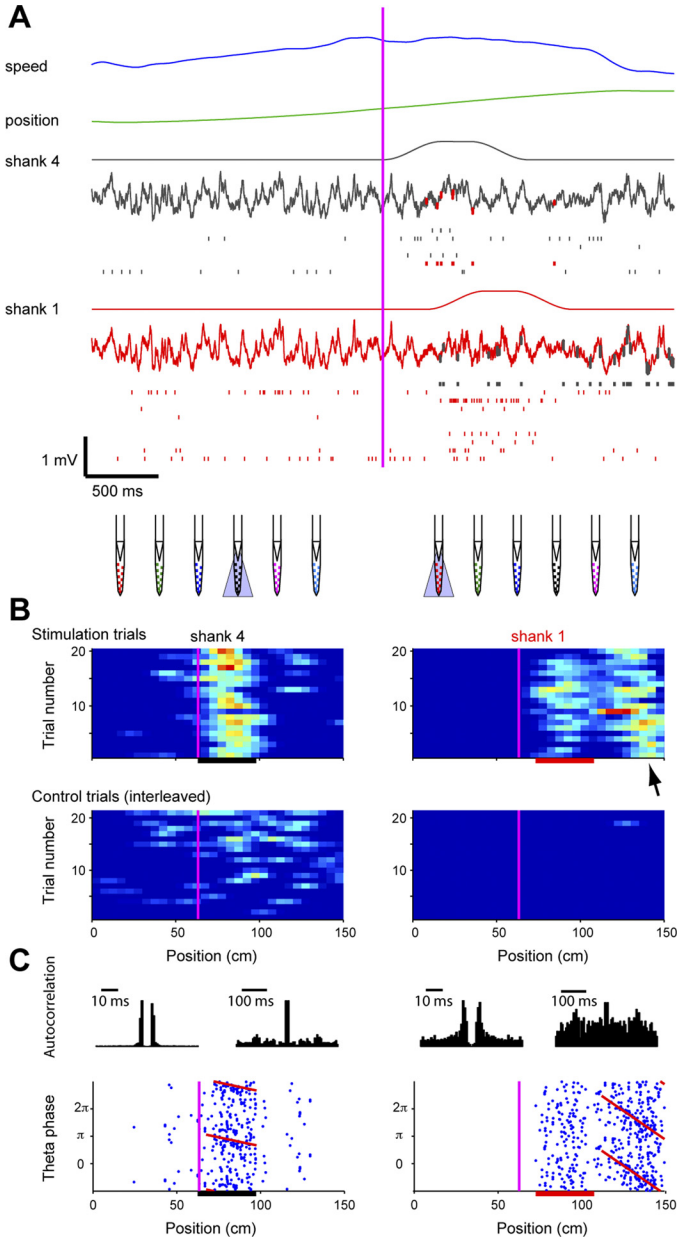


Fig. 8. Closed-loop spatiotemporal photostimulation by diode probes on the linear track (rat CA3c). *A*: on alternating left-to-right runs, 2 shanks were illuminated sequentially for 1 s, starting at a predetermined position (magenta lines in all panels). For each shank (*4*, black; *1*, red), traces show light intensity (*top*) and wideband signal on 1 recording site (1–5,000 Hz; *bottom*); tick marks below indicate spike times for all simultaneously recorded units (*shank 4*, 6 units; *shank 1*, 10 units). Ranges: speed: 0–51 cm/s; position: 0–150 cm; light intensity, 0–0.1 mW/mm$^2$. *B*: examples of light-induced position-related spiking (*left*: *shank 4*, red unit from *A*; peak firing rate, 23 spikes/s; *right*: *shank 1*, black unit, peak firing rate, 28 spikes/s). Here and in *C*, horizontal bars indicate the average position of the animal during photostimuli. Note consistent position-related firing in both cases and induction of a novel place field for the *shank 1* unit (arrow). *C*: interaction between light-driven spiking and native $\theta$-oscillations. *Top*: autocorrelation histograms for the pyramidal cells in *B*; side lobes indicate $\theta$ (~8 Hz) modulation. *Bottom*: $\theta$-phase (0: peak) of spikes shifts as a function of position during stimulation trials, illustrating an interaction between light-induced and network-controlled effects.

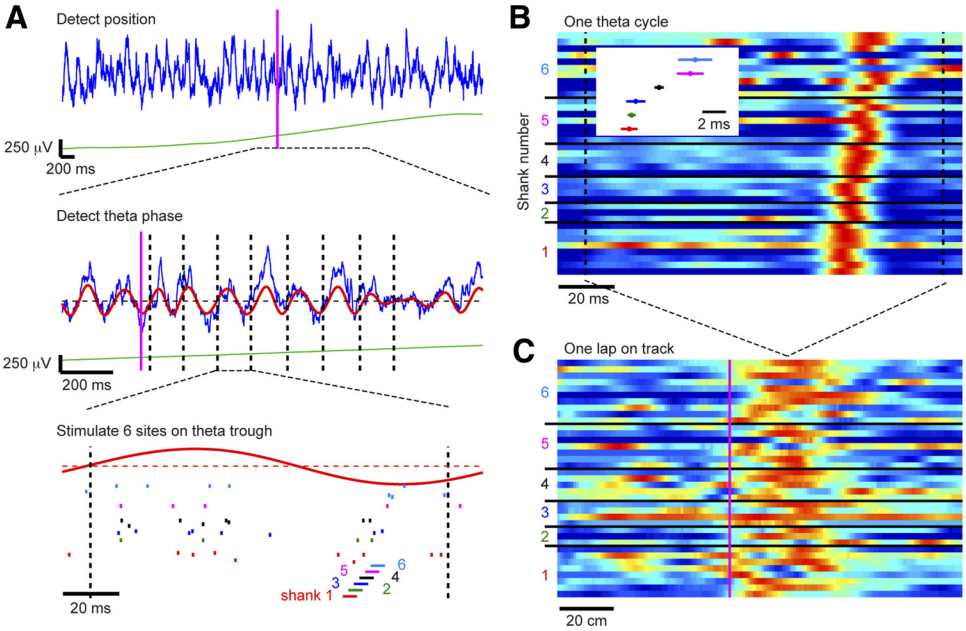


Fig. 9. Spatiotemporal photostimulation evoked by brain patterns in the behaving rat. *A*: as the animal (wild-type rat injected with CAG-ChR2 in the dentate gyrus) was running back and forth on the linear track, $\theta$-phase was determined in real time (dashed black lines here and in *B*: 0-crossing events). Starting from a predetermined position (magenta), on alternating right-to-left laps, a train of 6 brief light pulses was delivered at 6 separate sites (shifted horizontal bars, *bottom*) during $\theta$-troughs. Each row in the raster plot represents the spiking activity of 1 unit, colored according to the shank by which it was recorded. *B*: closed-loop stimulation resulted in precise spatiotemporal spiking within each individual $\theta$-cycle. Each row corresponds to the 1-ms binned PSTH of 1 unit recorded by 1 of the 6 shanks, averaged over 104 $\theta$-cycles, smoothed (Gaussian, SD = 5 ms), and scaled to 0–1. *Inset*: relative activity times of units recorded at the different shanks (medians). *C*: on a broader space and time scale, cells also exhibited position-related spiking. Each row corresponds to the scaled difference between stimulation/control position-related firing of 1 unit.

part of the track so that the firing induced by the weak multisite photostimuli was correlated with the spatial position of the animal (Fig. 9*C*) as well as with the $\theta$-phase, mimicking activity of place cells in the rat hippocampus. Synthetic patterns of neurons active at multiple parts of the environment will enable testing of the interplay between induced neuronal activity and plasticity in freely behaving animals.

## DISCUSSION

The recent rapid progress of optogenetic techniques enabled precise temporal control of neurons and populations (Deisseroth 2011; Fenno et al. 2011). Although the development of novel opsin types and improved cell-specific expression (Fenno et al. 2011; Zhao et al. 2011) can refine the influence of intracerebral illumination, specialized hardware is needed to enable independent control of multiple sites in the brains of freely moving animals. The methods introduced here complement genetic techniques by providing the high-resolution spatial control necessary for analyzing local circuits in freely behaving animals. The combination of miniature diodes, optical fibers, and high-resolution recording arrays with virus-injected wild-type or transgenic animals enables localized photostimulation and concurrent recording of the same cells at multiple brain sites independently and simultaneously. Since there are no bulky optical connections to the headstage, these arrays can be used in freely moving and/or behaving animals. Because the optical fibers are located very close to the recording electrodes, a small amount of light, obtained by efficient diode-fiber coupling, is sufficient for achieving robust control of local neurons. This enables driving small diodes with low currents, avoiding bulky heat sinks and collimating optics, preventing optical artifacts and spike superposition, and limiting the spatial extent of the photostimulus effect to a relatively small number of neurons, which are concurrently monitored by the extracellular electrodes.

For some applications, the use of spatially restricted photostimulation for localized neuronal control is actually a limitation. For instance, in experiments requiring synchronous control of an entire structure, the spatial extent of light stimulation should be two to three orders of magnitude higher than the ~0.001 $mm^3$ that can also be monitored electrophysiologically by a multisite shank of a silicon probe (Buzsáki 2004). Higher spatial coverage is readily achieved by using larger fibers and/or non-Lambertian light sources such as compact laser diodes (Fig. 6). For instance, coupling a laser diode to a 200-$\mu$m fiber yields ~5 mW of light at the end of the fiber. This yields intensities similar to those obtained with diode-pumped solid-state (DPSS) lasers and provides spatial coverage on the order of 0.1 $mm^3$ per diode-fiber assembly while maintaining high light intensity, low driving currents, and small device size, thereby enabling implantation and use in freely moving animals. Alternatively, if the goal is to generate activity patterns in a large volume of brain sequentially or synchronously, multiple light sources coupled to small-diameter fibers can be used (Figs. 7–9). Thus the specific light sources and fibers should be tailored to the scientific question at hand.

Although often a desired strategy, there are several disadvantages of using large-core optical fibers coupled with strong light sources. First, in some applications of large-core optical fibers glued onto silicon probes (Kravitz et al. 2010), units could not be recorded by recording sites closer than 200 $\mu$m from the fiber tip, supposedly because the large cleaved fiber caused local damage and/or ischemia. Second, strong light of any wavelength carries considerable energy that is dissipated in the form of heat as photons are scattered and absorbed in brain tissue. Local heating has a mixed de-/hyperpolarizing effect on neuronal activity (Shen and Schwartzkroin 1988; Thompson et al. 1985), which may confound and/or limit the effect of optogenetic manipulations. Third, high-intensity light may generate photoelectrical artifacts manifested as LFP deflections (Cardin et al. 2010; Han et al. 2009; Kravitz et al. 2010) and cause synchronous activation of nearby neurons (Royer et al. 2010), limiting the interpretability of induced LFP patterns and the use of spike-sorting techniques. These issues were previously addressed in part by coupling small-core fibers to DPSS

lasers driven at low power (Royer et al. 2010), but since the number of fibers a freely moving animal can be tethered to is limited (1–2 for small rodents), the range of scientific questions that could be addressed was restricted. The methods introduced here enable independent multisite optical stimulation and address these issues by using small-diameter fibers ending with a point (thereby minimizing local ischemia/neuronal damage) emitting weak light (minimizing heat transfer, light artifacts, and synchronous activation) at a path perpendicular (or parallel, in the case of tetrodes) to the recording sites (thereby further reducing and abolishing light artifacts).

Regardless of the light intensity used, these devices open the possibility to tackle scientific questions that were not addressable in the past. Even a single tethered optic fiber limits movement if the animal turns in the same direction multiple times. Although a fiber commutator is a potential solution for a single fiber, two or more fibers have serious constraints on movement; these constraints can be alleviated by eliminating the need for tethered glass fibers. Indeed, diode probes enable experiments with behaving animals in which the number of illuminated and monitored brain areas exceeds the practical limit for the number of tethered fibers. These devices can be used to generate and monitor arbitrary spatiotemporal activity patterns in deep structures of the intact brain, a long-sought goal difficult to achieve with other recently developed optical stimulation techniques (Anikeeva et al. 2011; Grossman et al. 2010; LeChasseur et al. 2011; Royer et al. 2010; Wentz et al. 2011). Moreover, as shown here, diode probes can be combined with real-time signal processing in freely moving animals to probe the spatial memory/navigation system, study short-term modifications, and generate unique network rhythms. Localized closed-loop activation/silencing can be triggered by spikes of single neurons, combination of predetermined spike patterns of multiple cells, behavioral parameters, and/or selected features of LFPs (Figs. 7–9). Other experiments are clearly possible. For instance, relationships between spike timing and behavior can now be probed causally in performing animals by local jittering of spiking, modifying the correlation structure of the network, and/or dissociating input and output of multiple local circuits.

There are multiple possible extensions of the diode-probe technology. Because of the small size and weight of the diode-fiber assemblies, any animal that can be implanted with an extracellular electrode and modified genetically can also be implanted with a diode-probe array. Because the diode-probe arrays require only electrical connections, they can be used wirelessly (Wentz et al. 2011), enabling recording and stimulation experiments with, for instance, freely moving birds and/or long-term naturalistic experiments with larger animals while permitting precise, large-scale, spatiotemporal control of neuronal activity. Finally, microelectromechanical systems (MEMS) technology can be used to integrate diode dies with optical waveguides embedded in the shanks of a silicon probe (Zorzos et al. 2010), yielding yet smaller devices and scaling up the number of light sources.

## APPENDIX: LIGHT INTENSITY ATTENUATION IN BRAIN TISSUE

To estimate the light intensity (power/area) at various distances from the fiber tip, two measurements were made: power attenuation and geometric dispersion. Light power was measured as a function of brain tissue thickness and source wavelength. For that purpose, a piece of freshly acquired brain slice, 2–3 mm thick, was glued slightly above the bottom of a transparent plastic container with 0.1 M PBS, and a calibrated photosensor (S130A; Thorlabs) was placed immediately below the container. Fifty-micrometer core optical fibers (NA, 0.22; AFS50/125Y; Thorlabs) were coupled to light sources (blue: 465-nm LED, APA1606PBC/Z, Kingbright; 470-nm LED, LB-P4SG, OSRAM; 473-nm, 50-mW DPSS laser, Dream Lasers; orange: 589-nm, 50-mW DPSS laser, Dream Lasers; red: 639-nm, 10-mW laser diode, HL6358MG, Opnext), mounted on a micromanipulator, and gradually advanced through the brain at small (10–200 $\mu$m) increments. This approach yielded a measure of the total light power ($P$) as a function of distance ($d$) through brain tissue, with the distance attenuation due to absorption and scattering. The power of light at each distance $P(d)$ was divided by $P(0)$, the power without a brain above the sensor (which was always identical to the power measured as the fiber exited the brain from below) and fitted by a $\eta_{scatter} = P(d)/P(0) = 1/(s \cdot d + 1)$ scattering model (Aravanis et al. 2007). Although the model consistently overestimated power at distances >1 mm, power at shorter distances was well-approximated ($r^2 > 0.98$ in all cases). The fit did not depend on tip morphology (cleaved or pointed), source power, or the brain region used, although scattering was slightly higher (5–10%) in nonfresh tissue. The mean (± SE) scattering coefficients depended on wavelength and were (Fig. 3*A*, *bottom left*): blue light, 7.18 ± 0.17; orange, 4.37 ± 0.15; and red, 3.44 ± 0.05. For blue light, the current value is smaller than previously reported values (10.3 for the rat brain; Aravanis et al. 2007). The mismatch could be explained by the slightly different testing conditions. In previous measurements, light was shined through brain slices, which causes reflective losses and may result in a higher calculated spatial attenuation. In any event, estimates of spatial attenuation of light intensity (see below) were similar regardless of the precise number used (<10% change in the range of 6–9 for blue light; 2.5–4.5 for red light).

Next, the geometric dispersion of light was estimated. For an idealized cleaved fiber with radius $r_0$ and numerical aperture $NA_{out}$, light emission can be approximated by a cone with an angle given by $\sin\alpha = NA_{out}/n_{out}$, where $n_{out}$ is the RI of the brain tissue (1.35–1.37; Binding et al. 2011; Fig. 3*A*, *top left*). Thus the area of the cone cross-section depends on the $d$ from the fiber tip, $A(d) = \pi(r_0 + d\tan\alpha)^2$. If the distribution of light at each distance is assumed uniform, then $\Phi_{geometry}$ can be approximated analytically as a function of the axial distance ($d$) from the fiber tip: $\Phi(r,d) = 1/A(d)$ when $r \leq r_0 + d\tan\alpha$; $\Phi(r,d) = 0$ otherwise. The light intensity at each point is then $I(r,d) = P(d) \cdot \Phi(r,d)$ (Fig. 3*A*, *right*). However, for a realistic multimode fiber, light does not travel at a single mode, not all rays are meridional, and therefore some light may be reflected at the tip. This breakdown is even more pronounced for a fiber etched to a point and driven by a Lambertian source (e.g., an LED), limiting the potential effectiveness of ray tracing techniques in approximating the geometric distribution of light at the tip. For these reasons, a more direct approach was also used by visualizing the light and measuring its distribution empirically.

Fibers, coupled to blue LEDs, were placed in a 30 $\mu$M fluorescein (in PBS) bath (2-mm height), and the fluorescent

emission was photographed by a Zeiss camera via the FITC filter of an Olympus microscope (Godwin et al. 1997; Fig. 3*B*, *top left*; note that this is only a proxy to the real geometric distribution of light in the brain since scattering may contribute to the geometric distribution, especially at short wavelengths). The square root of this image is essentially a two-dimensional (2-D) map of the light distribution at each $d$ and $r$ from the fiber tip, $H(r,d)$. From this map, a 2-D map of the geometric dispersion of light, $\Phi(r,d)$, was derived as follows. Assuming radial symmetry around the center of the fiber, the image was first aligned along the optical axis, and $H$ was averaged across this axis to reduce measurement noise. The geometric dispersion factor was then computed as $\Phi(r,d) = V(r,d)/[A(r,d)\cdot\sum V(r,d)]$ when $r \leq r_{\max}(d)$; $\Phi(r,d) = 0$ otherwise; where $A(r,d)$ is the area of the ring of $r$ at $d$, $V(r,d)$ is the volume of that ring, $A(r,d)\cdot H(r,d)$, and summation is over all radial elements that have nonnegligible intensity [i.e., contribute to the 99% support of the cross-section, $r_{\max}(d)$]. Note that for a uniform distribution, $H(r,d) = H(d)$ and $\Phi(r,d) = 1/\sum A(r,d)$. The resulting geometric attenuation and intensity maps are shown in Fig. 3*B*, *middle* and *right*.

The above procedure was verified in two ways. First, image processing was repeated for a cleaved fiber; this yielded geometric dispersion maps similar to the analytical ones, with the exception of higher attenuation at the edges of the light cone. Second, in a complementary (and computationally simpler) approach, the effective NA at fiber output, $NA_{out}$, was estimated by robust linear regression of the radius of support, $r_{\max}$, on the distance from the fiber tip, $d$. For fibers etched to a point, the divergence angles obtained were $16.3 \pm 0.3°$ ($r^2 = 0.97$), corresponding to an effective $NA_{out}$ of 0.37 (Fig. 3*B*, *top left*). By assuming a uniform distribution at each distance, a geometric dispersion factor $\Phi$ was obtained analytically (as for an ideal cleaved fiber); the resulting estimates were similar to those obtained using image processing (<5% differences).

## ACKNOWLEDGMENTS

We thank Ed Boyden for providing the ChR2-GFP construct, Karl Deisseroth for providing the Halo construct, Ronny Eichler for technical assistance, Shigeyoshi Fujisawa for providing transgenic mice, Kenji Mizuseki for insightful comments, and Karel Svoboda for providing the ChR2-tdTomato construct.

## GRANTS

This study was supported by National Institutes of Health Grants NS-034994 and MH-54671, National Science Foundation Grant SBE 0542013, and the J. D. McDonnell Foundation (G. Buzsáki) and Rothschild Foundation, Human Frontier Science Program Grant LT-000346/2009-L, and the Machiah Foundation (E. Stark).

## DISCLOSURES

No conflicts of interest, financial or otherwise, are declared by the author(s).

## AUTHOR CONTRIBUTIONS

E.S., T.K., and G.B. designed research and wrote the manuscript; E.S. designed and manufactured the diode probes and all other components, conducted surgeries, and performed the experiments.

## REFERENCES

**Airan RD, Thompson KR, Fenno LE, Bernstein H, Deisseroth K.** Temporally precise in vivo control of intracellular signaling. *Nature* 458: 1025–1029, 2009.

**Anikeeva P, Andalman AS, Witten I, Warden M, Goshen I, Grosenick L, Gunaydin LA, Frank LM, Deisseroth K.** Optetrode: a multichannel readout for optogenetic control in freely moving mice. *Nat Neurosci* 15: 163–170, 2011.

**Aravanis AM, Wang LP, Zhang F, Meltzer LA, Mogri MZ, Schneider MB, Deisseroth K.** An optical neural interface: in vivo control of rodent motor cortex with integrated fiberoptic and optogenetic technology. *J Neural Eng* 4: S143–S156, 2007.

**Bi GQ, Poo MM.** Synaptic modifications in cultured hippocampal neurons: dependence on spike timing, synaptic strength, and postsynaptic cell type. *J Neurosci* 18: 10464–10472, 1998.

**Binding J, Ben Arous J, Léger JF, Gigan S, Boccara C, Bourdieu L.** Brain refractive index measured in vivo with high-NA defocus-corrected full-field OCT and consequences for two-photon microscopy. *Opt Express* 19: 4833–4847, 2011.

**Boyden ES, Zhang F, Bamberg E, Nagel G, Deisseroth K.** Millisecond-timescale, genetically targeted optical control of neural activity. *Nat Neurosci* 8: 1263–1268, 2005.

**Braitenberg V, Schüz A.** *Cortex: Statistics and Geometry of Neuronal Connectivity*. Berlin: Springer, 1998.

**Buzsáki G.** Large-scale recording of neuronal ensembles. *Nat Neurosci* 7: 446–451, 2004.

**Cardin JA, Carlén M, Meletis K, Knoblich U, Zhang F, Deisseroth K, Tsai LH, Moore CI.** Targeted optogenetic stimulation and recording of neurons in vivo using cell-type-specific expression of Channelrhodopsin-2. *Nat Protoc* 5: 247–254, 2010.

**Chow BY, Han X, Dobry AS, Qian X, Chuong AS, Li M, Henninger MA, Belfort GM, Lin Y, Monahan PE, Boyden ES.** High-performance genetically targetable optical neural silencing by light-driven proton pumps. *Nature* 463: 98–102, 2010.

**Colvin J.** Coupling (launching) efficiency for a light-emitting diode, optical fibre termination. *Opto-electronics* 6: 387–392, 1974.

**Deisseroth K.** Optogenetics. *Nat Methods* 8: 26–29, 2011.

**Diester I, Kaufman MT, Mogri M, Pashaie R, Goo W, Yizhar O, Ramakrishnan C, Deisseroth K, Shenoy KV.** An optogenetic toolbox designed for primates. *Nat Neurosci* 14: 387–397, 2011.

**Fee MS, Mitra PP, Kleinfeld D.** Automatic sorting of multiple unit neuronal signals in the presence of anisotropic and non-Gaussian variability. *J Neurosci Methods* 69: 175–188, 1996.

**Fenno L, Yizhar O, Deisseroth K.** The development and application of optogenetics. *Annu Rev Neurosci* 34: 389–412, 2011.

**Fujisawa S, Amarasingham A, Harrison MT, Buzsáki G.** Behavior-dependent short-term assembly dynamics in the medial prefrontal cortex. *Nat Neurosci* 11: 823–833, 2008.

**Godwin DW, Che D, O'Malley DM, Zhou Q.** Photostimulation with caged neurotransmitters using fiber optic lightguides. *J Neurosci Methods* 73: 91–106, 1997.

**Gradinaru V, Thompson KR, Zhang F, Mogri M, Kay K, Schneider MB, Deisseroth K.** Targeting and readout strategies for fast optical neural control in vitro and in vivo. *J Neurosci* 27: 14231–14238, 2007.

**Gradinaru V, Zhang F, Ramakrishnan C, Mattis J, Prakash R, Diester I, Goshen I, Thompson KR, Deisseroth K.** Molecular and cellular approaches for diversifying and extending optogenetics. *Cell* 141: 154–165, 2010.

**Grossman N, Poher V, Grubb MS, Kennedy GT, Nikolic K, McGovern B, Berlinguer Palmini R, Gong Z, Drakakis EM, Neil MA, Dawson MD, Burrone J, Degenaar P.** Multi-site optical excitation using ChR2 and micro-LED array. *J Neural Eng* 7: 16004, 2010.

**Gunaydin LA, Yizhar O, Berndt A, Sohal VS, Deisseroth K, Hegemann P.** Ultrafast optogenetic control. *Nat Neurosci* 13: 387–392, 2010.

**Halassa MM, Siegle JH, Ritt JT, Ting JT, Feng G, Moore CI.** Selective optical drive of thalamic reticular nucleus generates thalamic bursts and cortical spindles. *Nat Neurosci* 14: 1118–1120, 2011.

**Han X, Qian X, Bernstein JG, Zhou HH, Franzesi GT, Stern P, Bronson RT, Graybiel AM, Desimone R, Boyden ES.** Millisecond-timescale optical control of neural dynamics in the nonhuman primate brain. *Neuron* 62: 191–198, 2009.

**Harris KD, Henze DA, Csicsvari J, Hirase H, Buzsáki G.** Accuracy of tetrode spike separation as determined by simultaneous intracellular and extracellular measurements. *J Neurophysiol* 84: 401–414, 2000.

**Huber D, Petreanu L, Ghitani N, Ranade S, Hromádka T, Mainen Z, Svoboda K.** Sparse optical microstimulation in barrel cortex drives learned behaviour in freely moving mice. *Nature* 451: 61–64, 2008.

**Hudson MC.** Calculation of the maximum optical coupling efficiency into multimode optical waveguides. *Appl Opt* 13: 1029–1033, 1974.

**Kravitz AV, Freeze BS, Parker PR, Kay K, Thwin MT, Deisseroth K, Kreitzer AC.** Regulation of parkinsonian motor behaviours by optogenetic control of basal ganglia circuitry. *Nature* 466: 622–626, 2010.

**LeChasseur Y, Dufour S, Lavertu G, Bories C, Deschênes M, Vallée R, De Koninck Y.** A microprobe for parallel optical and electrical recordings from single neurons in vivo. *Nat Methods* 8: 319–325, 2011.

**O'Keefe J, Nadel L.** *The Hippocampus as a Cognitive Map*. Oxford, UK: Oxford Univ. Press, 1978.

**O'Keefe J, Recce ML.** Phase relationship between hippocampal place units and the EEG theta rhythm. *Hippocampus* 3: 317–330, 1993.

**Potter RJ.** Transmission properties of optical fibers. *J Opt Soc Am* 51: 1079–1089, 1961.

**Royer S, Zemelman BV, Barbic M, Losonczy A, Buzsáki G, Magee JC.** Multi-array silicon probes with integrated optical fibers: light-assisted perturbation and recording of local neural circuits in the behaving animal. *Eur J Neurosci* 31: 2279–2291, 2010.

**Saleh B, Teich MC.** *Fundamental of Photonics*. New York: Wiley-Interscience, 2007.

**Schmitzer-Torbert N, Jackson J, Henze D, Harris K, Redish AD.** Quantitative measures of cluster quality for use in extracellular recordings. *Neuroscience* 131: 1–11, 2005.

**Shadlen MN, Newsome WT.** The variable discharge of cortical neurons: implications for connectivity, computation, and information coding. *J Neurosci* 18: 3870–3896, 1998.

**Shen KF, Schwartzkroin PA.** Effects of temperature alterations on population and cellular activities in hippocampal slices from mature and immature rabbit. *Brain Res* 475: 305–316, 1988.

**Thomson AM, Radpour S.** Excitatory connections between CA1 pyramidal cells revealed by spike triggered averaging in slices of rat hippocampus are partially NMDA receptor mediated. *Eur J Neurosci* 3: 587–601, 1991.

**Thompson SM, Masukawa LM, Prince DA.** Temperature dependence of intrinsic membrane properties and synaptic potentials in hippocampal CA1 neurons in vitro. *J Neurosci* 5: 817–824, 1985.

**Wentz CT, Bernstein JG, Monahan P, Guerra A, Rodriguez A, Boyden ES.** A wirelessly powered and controlled device for optical neural control of freely-behaving animals. *J Neural Eng* 8: 046021, 2011.

**West MJ, Slomianka L, Gundersen HJ.** Unbiased stereological estimation of the total number of neurons in the subdivisions of the rat hippocampus using the optical fractionator. *Anat Rec* 231: 482–497, 1991.

**Zhang F, Wang LP, Brauner M, Liewald JF, Kay K, Watzke N, Wood PG, Bamberg E, Nagel G, Gottschalk A, Deisseroth K.** Multimodal fast optical interrogation of neural circuitry. *Nature* 446: 633–639, 2007.

**Zhao S, Ting JT, Atallah HE, Qiu L, Tan J, Gloss B, Augustine GJ, Deisseroth K, Luo M, Graybiel AM, Feng G.** Cell type-specific channelrhodopsin-2 transgenic mice for optogenetic dissection of neural circuitry function. *Nat Methods* 8: 745–752, 2011.

**Zorzos AN, Boyden ES, Fonstad CG.** Multiwaveguide implantable probe for light delivery to sets of distributed brain targets. *Opt Lett* 35: 4133–4135, 2010.